2017

Characterization of the influence of external stimulus on protein-nucleic acid complex through multiscale computations

Agnivo Gosai
Iowa State University

Characterization of the influence of external stimulus on protein-nucleic acid complex through multiscale computations

by

Agnivo Gosai

A thesis submitted to the graduate faculty

in partial fulfillment of the requirements for the degree of

MASTER OF SCIENCE

Major: Mechanical Engineering

Program of Study Committee:
Pranav Shrotriya, Major Professor
Ganesh Balasubramanian
Sonal Padalkar
Marit Nilsen-Hamilton
Liang Dong

Iowa State University

Ames, Iowa

2017

TABLE OF CONTENTS

LIST OF FIGURES

LIST OF TABLES

ACKNOWLEDGMENTS

I would like to thank my committee chair, Prof. Pranav Shrotriya, and my committee members, Prof. Ganesh Balasubramanian, Prof. Sonal Padalkar, Prof. Liang Dong, and Prof. Marit Nilsen-Hamilton, for their guidance and support throughout the course of this research.

In addition, I would also like to thank my friends, colleagues, the department faculty and staff for making my time at Iowa State University a wonderful experience.

ABSTRACT

The concomitant detection, monitoring and analysis of biomolecules have assumed utmost importance in the field of medical diagnostics as well as in different spheres of biotechnology research such as drug development, environmental hazard detection and biodefense. There is an increased demand for the modulation of the biological response for such detection / sensing schemes which will be facilitated by the sensitive and controllable transmission of external stimuli. Electrostatic actuation for the controlled release/capture of biomolecules through conformational transformations of bioreceptors provides an efficient and feasible mechanism to modulate biological response. In addition, electrostatic actuation mechanism has the advantage of allowing massively parallel schemes and measurement capabilities that could ultimately be essential for biomedical applications.

Experiments have previously demonstrated the unbinding of thrombin from its aptamer in presence of small positive electrode potential whereas the complex remained associated in presence of small negative potentials / zero potential. However, the nanoscale physics/chemistry involved in this process is not clearly understood.

In this thesis a combination of continuum mechanics based modeling and a variety of atomistic simulation techniques have been utilized to corroborate the aforementioned experimental observations. It is found that the computational approach can satisfactorily predict the dynamics of the electrically excited aptamer-thrombin complex as well as provide an analytical model to characterize the forced binding of the complex.

CHAPTER 1. GENERAL INTRODUCTION

1.1 Electrically switchable smart biosensors

The key component of a biosensor is a biological material, such as an antibody, a membrane receptor, a single stranded nucleic acid, an enzyme or even a whole cell, which is usually immobilized on the surface of a suitable transducer. In this system, the biological material is responsible for a specific recognition of the analyte at the transducer surface and the transducer for the conversion of said recognition event into a processable signal. The selective and specific recognition of a given analyte is achieved by a biochemical reaction between said analyte and said biological material, that results either in the formation of a surface-bound affinity complex (affinity biosensors) or in the enzymatic conversion of the analyte into a product (catalytic biosensors). Detection and monitoring of biomolecules is invaluable not only in the field of medical diagnostics but also in biotechnology research, drug development, environmental monitoring, forensic investigations, and biodefense. The current state of the art nanoscale devices for the modulation of biological response demand sensitive and controllable transmission of external stimuli to biological systems. Electrostatic actuation for the controlled release/capture of biomolecules through conformational transformations of bioreceptors provides an efficient and feasible mechanism to modulate biological response. In addition, electrostatic actuation mechanism has the advantage of allowing massively parallel schemes and measurement capabilities that could ultimately be essential for biomedical applications.

The objective of the proposed research is to characterize the influence of external force on a surface bound or tethered nucleic acid conjugated with its target ligand protein. In

the research described in this thesis, the fifteen-nucleotide thrombin binding aptamer (TBA) has been chosen as the nucleic acid, with human alpha thrombin as the ligand protein.

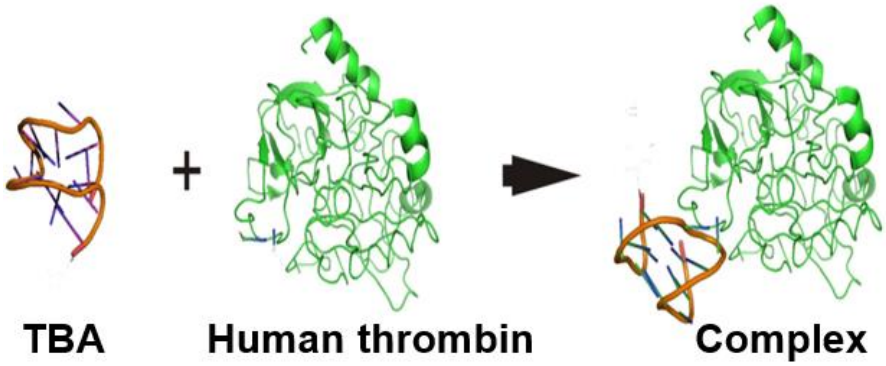

Figure 1 The TBA and thrombin complex

The central hypothesis of this study is that on application of external force or stimuli in the form of an electric field, the bound complex between TBA and thrombin changes and this configurational transition is controllable. To verify this hypothesis, experimental investigations have been carried out. In the present thesis, the hypothesis has been tested through computational approach using a blend of continuum scale and atomistic modeling. Following which a theory is developed to connect the experimental as well as simulation results from forced unbinding of TBA and thrombin complex.

1.2 Electric field induced dissociation of thrombin and aptamer complex

A stimuli sensitive surface that can bind/release specific biomolecules under application of external stimuli may be able to dynamically translate external stimuli into biochemical signals and efficiently transmit such signal into the biological systems. Such surfaces may be used to facilitate selective delivery of signaling chemicals, locate disease sites, repair or reprogram genetic information, and modulate biological system activity[1-3]. Electrostatic stimuli based smart surfaces have many advantages for communicating

information in device/biological interfaces. Integrated nanoscale devices governed by electrical mechanism are readily scalable, allowing fully reversible control, and massively parallel actuation and measurement capabilities[3]. Furthermore, the extensive infrastructure and technique developed for semiconductor processing can be applied for nanoscale fabrication and synthesis. However, electrical mechanisms with limited selectivity are generally not the natural mode of communication in biological systems. In contrast, biomolecules exhibit unparalleled nanoscale functionalities, such as detecting conformation changes, chemical modification and specific ligand binding, as well as implementing mechanical actuation, membrane signaling, chemical transport and catalysis[3, 4]. Hence smart surfaces that enable electrical field based modulation of biomolecular response can leverage these capabilities to influence biological behavior or enhance the functionality of artificial devices.

Self-assembled monolayers (SAM) of polymers that undergo conformational transitions due to changes in – thermal, ionic strength, optical or electrical – stimuli have been widely investigated to control and modify surface properties. Thermoresponsive polymer such as poly-N-isopropylacrylamide (PNIPAm), alters its conformational state on change of temperature to modulate protein adsorption and cell adhesion[5, 6]. Change in ionic strength or pH value has also been investigated as a means to regulate ligand binding and cellular adhesion on polyelectrolyte polymer covered surfaces (e.g. poly-2-dimethylamino-ethyl methacrylate (PDMAEMA)) through the shielding effect of surrounding ions[7, 8]. Nevertheless, it should be noted that thermoresponsive surface and polyelectrolyte brushes have limited applications in specific ligand recognition and protein absorption due to the nonspecific hydrophobic and columbic interaction[9, 10]. A number of recent studies have

investigated optical mechanism that governs responsive surfaces[11-13]. Photoresponsive surfaces with photocleavable 2-nitrobenzyl groups allow specific protein adsorption and cell adhesion through cleavage of functional group and succeed in the formation of specific cell patterns. However, the application of optical stimuli is supposed to induce a localized electron transfer and functional group cleavage[14], thus limiting the magnitude of conformational change and the ability to achieve reversible control.

Compared to previously mentioned mechanisms of modulation, application of electrostatic fields is a feasible and efficient way to generate substantial conformational transition in polar or charged molecules[15-17]. Formation of ionic double layer near the

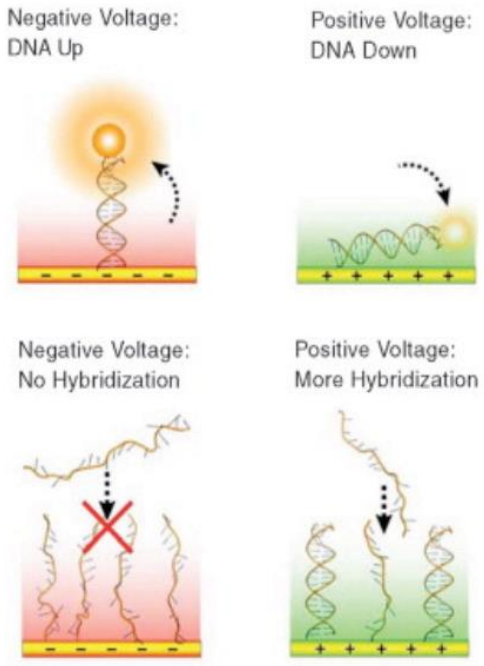

Figure 2 DNA actuation through electric field and effect on hybridization[18,19]

electrode surface leads to the generation of strong electrical fields within several nanometers, and an exponential decrease of electrical field strength beyond that range. This scenario implies that relatively low external voltages may induce considerable conformational transition on the polar or charged biomolecules near the electrode surface without any

detrimental effects on the system, which is very useful for modulating ligand sensing and binding. Rant et al.[18, 19]demonstrated that the conformation of short DNA oligomers immobilized on gold substrate with low grafting densities can be reversibly switched by the application of electrical fields.

Wong et al.[20] discovered that electrostatic fields can effectively influence self-assembly and hybridization of DNA. Positive voltage of 300 mV applied to single-strand DNA functionalized gold electrodes shows a three-fold enhancement in complementary DNA hybridization, while under negative voltage of -300mV the hybridization level decreases by an order of magnitude. Mendes et al. [21] utilized negative electrical potential to attract positively charged biotinylated oligolysine peptides (biotin-Lys-Lys-Lys-Lys-Cys,) onto gold electrode surface, and dramatically altered the binding activity between the biotin functionalized on the end of peptides and its counterpart neutravidin. Huang et.al.[22] adopted electrical field to generate conformational changes in TBA molecules immobilized on Au nanowire for ultrasensitive detection of fluorescent-labeled thrombin, and quantified the binding affinity between thrombin and its aptamer to be ~30 nM in the titration assay, which is within the previously reported range (25 – 200 nM) [23], and comparable to high binding affinity between antigen and antibody which is usually less than 100nM.

In the 2nd chapter of the thesis, the influence of an external electric field on the TBA-thrombin complex has been computationally investigated. It is shown that moderate electrical fields can be utilized to change the binding behavior between thrombin and aptamer, and thus realize the electrostatic actuation based modulation of the stimuli responsive surface.

1.3 Analytical model for correlating experimental and computational characterization of forced unbinding of TBA-thrombin complex

In the development of an electrically switchable smart surface the characterization of the interaction forces between biomolecules becomes a key factor to determine molecular binding specificity and stability. Low binding forces between a complementary pair of biomolecules may result in an unstable nanostructure or a lack of sensitivity in the sensor performance. It is thus important to measure the force of interaction between a pair of biomoelcules to thoroughly characterize the binding mechanism of the pair.

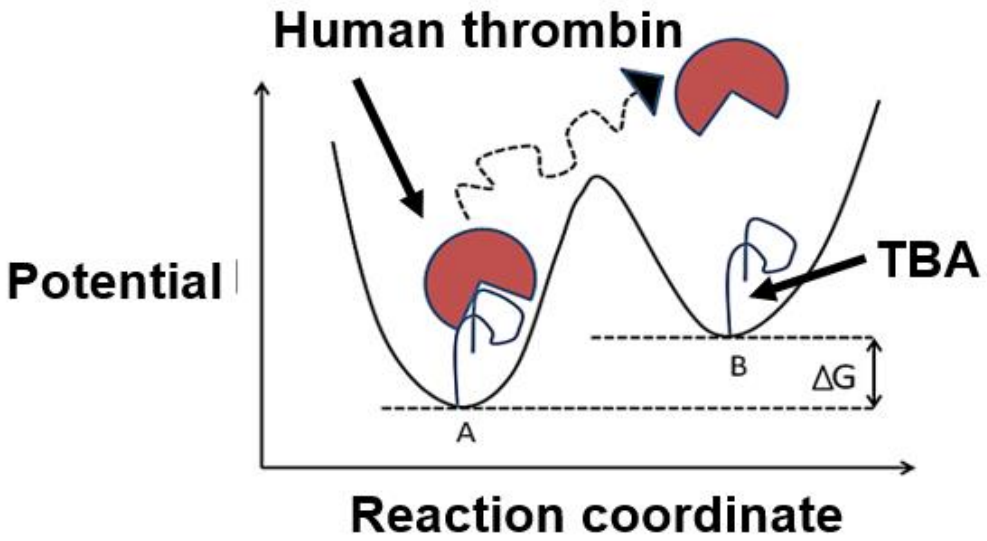

Figure 3 The dissociation of TBA and thrombin complex due to application of an energy ΔG

Dynamic Force Spectroscopy (DFS) has been utilized to measure dissociation forces between specific complementary chemical and biological molecules [24-26]. Analysis of the unbinding forces reveals remarkable insight into energy consumption, binding kinetics and thermodynamic parameters for the molecular bonds [27]. These advantages make it a useful tool for probing the nature and mechanism of biomolecular interactions and cellular

adhesion. However, DFS experiments are limited to slow loading rates. Molecular dynamics simulations could be used to simulate the unbinding response but constraints in computational resources force the simulations to orders of magnitudes faster than experimental conditions. Hence as a measure to connect these two extremes, an analytical model based on a general framework of stochastic processes and rate theory is utilized [28-30]. A comparison between experimental and computational DFS-based analysis of the specific binding between thrombin and its DNA aptamer in order to characterize the DFS response over a significantly larger loading rate than previously reported, is presented. It should be noticed that explicit measurement and characterization of the binding force between thrombin-aptamer complex and investigation of the kinetics which governs the molecular binding could provide in-depth information and insights on the electrostatic actuation based modulation of the conformation and binding behavior of biomolecules, which would facilitate the functional design of a biotic-abiotic interface.

1.4 Thesis organization

Chapters 2 and 3 correspond to the research goals identified and described above. Specifically, chapter 2 details the effect of electrical field on the association/dissociation of the TBA and thrombin complex, which forms a basis for the experimental validation. Chapter 3 describes the DFS experiments to probe the binding of the complex and provides an analytical model to connect the experimental observations with MD simulations. Finally, chapter 4 summarizes all of the conclusions drawn from the thesis and outlines a plan for the future work on this topic. Appendix A provides a detailed explanation of the modeling described in chapter 1, whereas, Appendix B details particular aspects of the simulations discussed in chapter 3.

References

1. Kuroki, H., Tokarev, I. & Minko, S. Responsive Surfaces for Life Science Applications. *Annu Rev Mater Res* **42**, 343-372 (2012).
2. Mendes, P.M. Stimuli-responsive surfaces for bio-applications. *Chem Soc Rev* **37**, 2512-2529 (2008).
3. Wong, I.Y., Almquist, B.D. & Melosh, N.A. Dynamic actuation using nano-bio interfaces. *Mater Today* **13**, 14-22 (2010).
4. Wong, I.Y. & Melosh, N.A. An Electrostatic Model for DNA Surface Hybridization. *Biophysical Journal* **98**, 2954-2963 (2010).
5. Burkert, S. et al. Protein resistance of PNIPAAm brushes: application to switchable protein adsorption. *Langmuir* **26**, 1786-1795 (2010).
6. Akiyama, Y., Kikuchi, A., Yamato, M. & Okano, T. Ultrathin poly(N-isopropylacrylamide) grafted layer on polystyrene surfaces for cell adhesion/detachment control. *Langmuir* **20**, 5506-5511 (2004).
7. Chiang, E.N., Dong, R., Ober, C.K. & Baird, B.A. Cellular responses to patterned poly(acrylic acid) brushes. *Langmuir* **27**, 7016-7023 (2011).
8. Ballauff, M.B., O. Polyelectrolyte brushes. *Current Opinion in Colloid & Interface Science* **11**, 316 - 323 (2006).
9. Hianik, T., Ostatna, V., Sonlajtnerova, M. & Grman, I. Influence of ionic strength, pH and aptamer configuration for binding affinity to thrombin. *Bioelectrochemistry* **70**, 127-133 (2007).
10. Hianik, T., Ostatna, V., Zajacova, Z., Stoikova, E. & Evtugyn, G. Detection of aptamer-protein interactions using QCM and electrochemical indicator methods. *Bioorganic & Medicinal Chemistry Letters* **15**, 291-295 (2005).
11. Liu, D.B.X., Y. Y.; Shao, H. W.; Jiang, X. Y. Using Azobenzene-Embedded Self-Assembled Monolayers To Photochemically Control Cell Adhesion Reversibly. *Angewandte Chemie-International Edition* **48**, 4406 - 4408 (2009).
12. Nakanishi, J. et al. Spatiotemporal control of migration of single cells on a photoactivatable cell microarray. *J Am Chem Soc* **129**, 6694-6695 (2007).
13. Auernheimer, J., Dahmen, C., Hersel, U., Bausch, A. & Kessler, H. Photoswitched cell adhesion on surfaces with RGD peptides. *J Am Chem Soc* **127**, 16107-16110 (2005).
14. Willner, I.K., E. Bioelectronics: From Theory to Applications. (Wiley-VCH Verlag GmbH & Co., 2005).
15. Lahann, J. et al. A reversibly switching surface. *Science* **299**, 371-374 (2003).
16. Ma, X. & Shrotriya, P. Molecular Dynamics simulation of electrical field induced conformational transition and associated frictional performance of monomolecular films. *J Phys D Appl Phys* **45** (2012).
17. Ma, X. & Shrotriya, P. Molecular Dynamics Simulation of Conformational Transition and Frictional Performance Modulation of Densely Packed Self-Assembled Mono layers Based on Electrostatic Stimulation. *Langmuir* **31**, 6729-6741 (2015).
18. Rant, U. et al. Dynamic electrical switching of DNA layers on a metal surface. *Nano Lett* **4**, 2441-2445 (2004).

19. Rant, U. et al. Switchable DNA interfaces for the highly sensitive detection of label-free DNA targets. *Proceedings of the National Academy of Sciences of the United States of America* **104**, 17364-17369 (2007).
20. Wong, I.Y. & Melosh, N.A. Directed Hybridization and Melting of DNA Linkers using Counterion-Screened Electric Fields. *Nano Lett* **9**, 3521-3526 (2009).
21. Yeung, C.L. et al. Tuning Specific Biomolecular Interactions Using Electro-Switchable Oligopeptide Surfaces. *Advanced Functional Materials* **20**, 2657-2663 (2010).
22. Huang, S.X. & Chen, Y. Ultrasensitive fluorescence detection of single protein molecules manipulated electrically on Au nanowire. *Nano Lett* **8**, 2829-2833 (2008).
23. Bock, L.C., Griffin, L.C., Latham, J.A., Vermaas, E.H. & Toole, J.J. Selection of Single-Stranded-DNA Molecules That Bind and Inhibit Human Thrombin. *Nature* **355**, 564-566 (1992).
24. Florin, E.L., Moy, V.T. & Gaub, H.E. Adhesion Forces between Individual Ligand-Receptor Pairs. *Science* **264**, 415-417 (1994).
25. Oncins, G., Vericat, C. & Sanz, F. Mechanical properties of alkanethiol monolayers studied by force spectroscopy. *J Chem Phys* **128** (2008).
26. Strunz, T., Oroszlan, K., Schafer, R. & Guntherodt, H.J. Dynamic force spectroscopy of single DNA molecules. *P Natl Acad Sci USA* **96**, 11277-11282 (1999).
27. Flyvbjerg, H. Physics of bio-molecules and cells = Physique des biomolécules et des cellules: Les Houches session LXXV. (EDP Sciences; Springer, Les Ulis, 2002).
28. Evans, E. & Ritchie, K. Dynamic strength of molecular adhesion bonds. *Biophysical journal* **72**, 1541-1555 (1997).
29. Grubmuller, H., Heymann, B. & Tavan, P. Ligand Binding: Molecular Mechanics Calculation of the Streptavidin-Biotin Rupture Force. *Science (New York, N.Y.)* **271** (1996).
30. Heymann, B. & Grubmüller, H. AN02/DNP-hapten unbinding forces studied by molecular dynamics atomic force microscopy simulations. *Chem Phys Lett* **303**, 1-9 (1999).

CHAPTER 2. ELECTRICAL STIMULUS CONTROLLED BINDING/UNBINDING OF HUMAN THROMBIN-APTAMER COMPLEX

Agnivo Gosai[a,1], Xiao Ma[1], Ganesh Balasubramanian[1] and Pranav Shrotriya[*,1]

Modified from a paper published in *Scientific Reports*

2.1 Abstract

The binding/unbinding of the human thrombin and its 15-mer single stranded DNA aptamer, under the application of external stimulus in the form of electrostatic potential / electric field, is investigated by a combination of continuum analysis and atomistic molecular dynamics simulation. In agreement with the experiments that demonstrate the influence of electrostatic potential on the thrombin/aptamer complex, our computations show that the application of positive electric field successfully unbinds the thrombin from the aptamer. Results from umbrella sampling simulations reveal that there is a decrease in the free energy of binding between the thrombin and aptamer in presence of positive electric fields. Hydrogen bonding and non-bonded interaction energies, and hence the free energy of binding, between the thrombin and its aptamer reduce as the applied electric field is shifted from negative to positive values. Our analyses demonstrate that application of electrical stimulus modifies the molecular interactions within the complex and consequently, electrical field can be used to modulate the association between the thrombin and its aptamer.

[a] Primary researcher and author
[1] Department of Mechanical Engineering, Iowa State University, Ames, IA 50010
[*] To whom correspondence should be addressed, Email: shrotriy@iastate.edu

2.2 Introduction

Structural and functional biotic-abiotic nanoscale interfaces are very promising for applications in highly sensitive, biocompatible and flexible bio-sensors and actuators. Their potential use in biomedical and biomechanical sciences include, for instance, modulation of biological systems and biomolecular activity, disease detection as well as reprogramming of genetic information [1]. However, the on-demand actuation of the system components through efficient stimulation of the biotic-abiotic interface is a challenge. Amongst the different mechanisms employed to transmit stimulus, some of the widely used methods include variable electrolyte strength [2], temperature control [3] and electron transfer as a result of redox reactions [4]. The practice of actuating biomolecules by electric field has been gaining interest primarily inspired by earlier findings of the influence of electrostatic field on the self-assembly and hybridization of DNA [5-7], and the conformational switching of short DNA oligomers immobilized at low grafting densities [8, 9].

DNA aptamers used in biomedical applications, such as drug design, due to their highly specific biological activities, can potentially replace certain antibodies. They are particularly advantageous for sensors and biomedical device components because they (1) are small in size, (2) demonstrate high specificity for their receptors and (3) can be utilized for target species detection and selection of various biomolecules especially for biomedical material and drug design [10, 11]. Thrombin is a catalytic enzyme that plays a key role during blood coagulation by synthesizing fibrin from fibrinogen and has a wide range of health effects in the human body [12]. The thrombin binding aptamer (TBA), one of the most studied synthetic oligonucleotides, shown in Figure 1(a), is a single strand (ss) DNA with the sequence GGTTGGTGTGGTTGG [13, 14]. TBA shows the G-quadruplex structure consisting

of two planar G-quartets connected by two intervening TT and one TGT loop [15-18]. The G-quadruplex is stabilized through cation binding in its central binding site located between the two quadruplex planes. In addition to the active site, thrombin is characterized by two binding sites, exosite I and exosite II. The exosite I is known as the fibrinogen recognition site and the exosite II as the heparin binding site. These exosites are positively charged moieties in physiological pH and thus have the propensity of binding to negatively charged ligands, like the aptamer [11, 13]. The two lateral TT loops of TBA bind with exosite I whereas the TGT loop has been associated with exosite II [19]. The enzymatic activity of thrombin is inhibited when bound to TBA, due to fibrinogen blocking, facilitating its potential role as an anticoagulant.

The functions of a protein depend directly on its structure, which is susceptible to applied external stimuli such as variations in: electromagnetic field, microwave radiation, temperature, pressure and pH. The observation of protein configurational change, as verified experimentally, through simulations is a challenging task, as such processes span over longer time scales of minutes whereas classical molecular dynamics (MD) simulations are in the order of much shorter timescales (~ 10^{-9} s or nanoseconds or ns). Nevertheless, atomistic simulations provide a strategy to deterministically explore such molecular phenomena at a very high resolution[20, 21]. MD simulations have been previously employed to investigate the fundamental structural conformations of TBA in presence of cations (K^+, Na^+) [17]. Kim et al. carried out all atom replica exchange molecular dynamics (REMD) simulation to generate the free energy map and the folding mode of TBA [22]. Extremely long MD simulations of the order of a few microseconds concluded that the TGT loop of TBA stabilizes the entire structure of the complex in presence of the K+ ion and the TT loops are directly involved in

the binding with the thrombin [17]. Also, Kim et al. computed the potential of mean force (PMF) upon pulling the aptamer molecule from the binding mode (exosite I) of the TBA/thrombin complex [22].

We have previously reported the unbinding of TBA from thrombin in presence of an applied positive electric field through atomic force microscope (AFM) experiments [23]. The experimental setup consisted of a gold electrode which was functionalized by the thrombin aptamers (Figure 1(b)). The TBA was attached to the gold surface with a linker and was subsequently treated with thrombin to form the complex. On application of positive electrode potential the thrombin dissociates from the aptamer layer, while in presence of low negative electric fields the complex remains in its bound state [23]. In this paper, we investigate the effects of externally applied electrostatic potential on a film of TBA in salt solution using the Poisson Boltzmann equation (PBE) and calculate the free energy of binding between TBA and thrombin by MD simulations in presence of an applied electric field.

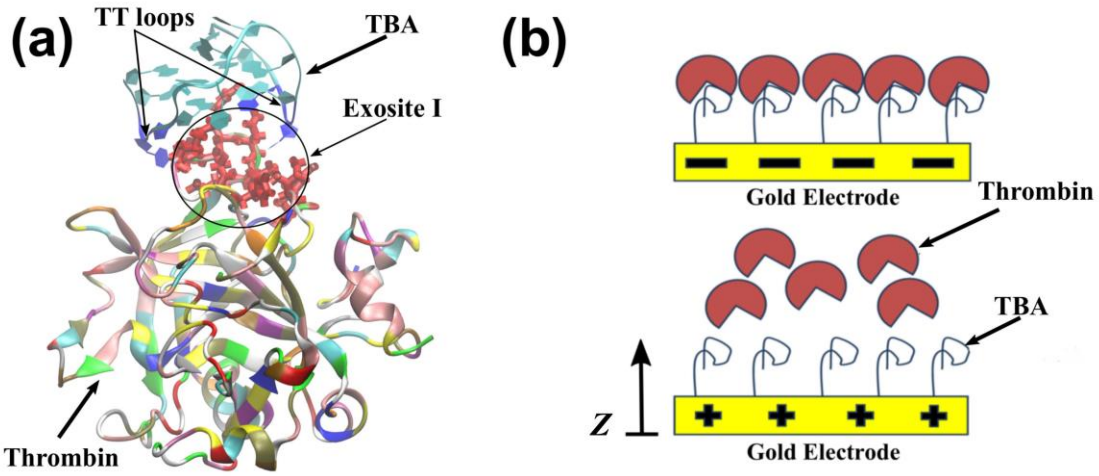

Figure 4: (a) Crystallographic structure (sourced from PDB entry 1HAO) of TBA/thrombin complex is presented by rendering in VMD [48]. The thymine residues (T3, T4, T12 and T13) of the TT loops of TBA are represented in blue whereas all the other DNA bases are shown in cyan. The exosite-I residues of thrombin are shown in red. **(b)** A cartoon describing the dissociation of TBA/thrombin complex on application of external stimulus[23], as observed experimentally, is shown.

The PBE equation is utilized to characterize the electric field in the nucleic acid layer, upon the application of electrode potential, whereas the MD simulations are used to investigate the effect of electric field on the aptamer-thrombin complex; the computational domains of these two approaches are marked out in Figure 1(b). We find that for positive electric fields the thrombin separates from the aptamer facilitated by a reduced free energy of binding.

2.3 Methods

Continuum modeling of the TBA layer

Single strand (ss) DNA can be effectively modeled by the polyelectrolyte brush theor y for sufficiently high (~ 10^{12}/nm^2) electrode grafting densities, wherein, the DNA strands are assumed to be stretched forming rod like structures. The charges due to the phosphate groups on the DNA bases are spaced in 0.4 nm intervals [7]. For the continuum analysis the TBA layer is assumed to be in a 0.1 M salt solution and we define a spatial direction *z* normal to the electrode surface (Figure 4(b)). The thrombin molecule is not included in this analysis. The DNA used in previous experimental work [23], consisted of the 15-mer TBA along with a 35 base long tail and a thiol end, forming the linker with the gold electrode (Figure 4(b)). The TBA has a G-quadraplex configuration resembling an armchair [29], as shown in Figure 4(a), hence, we approximate the charge distribution in DNA brushes with lower charge density over the height of 35-mer linker and higher charge density over the TBA layer. Initial calculations are done assuming the linker and TBA layer follow a rod-like structure. The effect of linker DNA condensation or folding is approximated by assuming lower heights for linker layers (Appendix A). The charge due to the 15 bases is uniformly distributed along the axial length of the TBA molecule (1.6 nm) as calculated from the structure in protein data bank (PDB) entry148D [29]. We also take into account the renormalization of the backbone negative charges of the DNA due to counterion condensation as described by Manning [30].

The charge density of the TBA is expressed as

$$\rho_{DNA} = \frac{e\sigma N f}{H}\theta(H - z) \qquad \textbf{(1)}$$

where, *e* is the electron charge, *f* the charging fraction calculated using Manning condensation theory, *N* the number of DNA bases, *H* the DNA layer height and θ is the

Heaviside step function. The aptamer sequence used in the experiments has, 35 nucleotides in the long tail and 15 nucleotides in the aptamer head. The charging fraction is calculated as $f = b/l_B$, where the Bjerrum length $l_B = e^2/\varepsilon k_B T$, where ε is relative permittivity of the medium, b the separation per charge, k_B the Boltzmann constant and the temperature, T = 300K. For our system, b = 0.4 nm and $l_B \sim 0.7$ nm, and hence $f = 0.57$. A 1 nm long charge neutral thiol linker molecule is also included in the model to mimic the thiol modification used to immobilize the aptamer with gold/thiol bond [28].

The counterion charge density is given by a modified Poisson-Boltzmann equation described by Borukhov et al. considering the finite size of ions [31]:

$$\rho_{ions} = \frac{2eC_{bulk}\sinh(\psi e/k_B T)}{1+2v\sinh^2(\psi e/2k_B T)}\theta(z\text{-}H) \quad \textbf{(2)}$$

where, C_{bulk} is the bulk counterion concentration, k_B the Boltzmann constant, ψ the electrostatic potential of the system, v the steric parameter limiting the ion concentration. v = 2 C_{bulk} × (ion radius)^3 [31]. The ion radius is 1.96 × 10^{-7} cm [7] . For the analysis counterions are excluded from the DNA layer as this provides the best agreement with experiments [7]. Equations (1) and (2) are used in the Poisson-Boltzmann equation and non-dimensionalized to obtain the second order differential equation governing the system:

$$\nabla^2\psi^*(z^*) = \beta\theta(H^* - z^*) + \frac{\sinh(\psi^*)}{1+2v\sinh^2(\psi^*/2)}\theta(z^* - H^*) \quad \textbf{(3)}$$

where ψ^* is the nondimensional electrostatic potential and H^* the non- dimensional DNA layer height. The electrostatic potential, ψ, and the spatial domain z, are non-dimensionalized by ($k_B T/e$) and the Debye length $\lambda_D = \sqrt{(8\pi l_B C_{bulk})}$ respectively; the dimensionless coefficient $\beta = Nf\sigma/2HC_{bulk}$. The governing equation is solved for boundary conditions of the external potential at electrode surface and zero electric field far away from the surface. The electrostatic potential distribution is computed for TBA layers with grafting densities varying

from $\sigma = 10^{11}$ cm^{-2} to $\sigma = 10^{12}$ cm^{-2} consistent with the experimental efforts of our group [23] and Stachowiak et al. [32] .

Molecular dynamics simulation of thrombin-TBA unbinding

The crystallographic structure of TBA/thrombin complex (Figure 1(a)) is obtained from the PDB entry 1HAO[33]. A combination of the force fields AMBER99SB, successfully employed to model proteins[34], and parmbsc0, which has been shown to improve ss DNA MD simulations[35], are used for our simulations on TBA/thrombin complexes [17, 22]in the GROMACS 4.6.7 package [36]. Following previously published literature [17], the Asp, Glu and His residues of thrombin were protonated according to the discussion by Ahmed et al. [37]. The TIP3P water model [38] is used to solvate the TBA/thrombin complex placed at the center of a rectangular 7.5 (x) nm × 7.5 (y) nm × 15 (z) nm) simulation box.; 26010 water molecules are added and 62 Na^+ and 51 Cl^- ions are included in the system to neutralize biomolecular charge and build up 0.1 M concentration.

The system is energy minimized using the steepest descent algorithm. Position restraints are applied to the TBA/thrombin complex and the system is equilibrated at 300 K and 1 bar with a time step of 2 fs (femtosecond) under (a) the canonical ensemble (NVT) using velocity rescaling thermostat [39] with coupling time constant of 0.1 ps for 1 ns, followed by (b) another 1 ns simulation under the isothermal-isobaric ensemble (NPT) using the Berendsen barostat [40] with coupling constant of 5.0 ps and the thermostat as before. The initial velocities are generated from a Maxwell distribution at 300 K at the start of the NVT equilibration. Subsequently, all position restraints are removed and a MD simulation is performed under the NPT ensemble for 50 ns employing the Nose-Hoover thermostat [41, 42]

with a coupling constant of 0.5 ps and the Parinello-Rahman barostat with coupling constant of 1.0 ps. In all the MD simulations the covalent bonds are constrained by the LINCS algorithm [43] and periodic boundary conditions are applied in all directions. All non-bonded interactions are cut off at 1.4 nm and an FFT grid density of 0.12 nm is used with the particle mesh Ewald (PME) method [44]. Atomic trajectories and thermodynamic data are recorded every 0.1 ps. Average structure of the thrombin-aptamer complex from the trajectory of the 50 ns production run is used for electric field MD simulations, where a time invariant constant magnitude electric field is applied along the (+) *z* axis. The TBA is position restrained to the energy minimized configurations as experimental results have shown that binding with thrombin protein stabilizes the G-quadraplex structure of the aptamer. Production simulations under the NPT ensemble spanning 5 ns are carried out to investigate the configurational changes of thrombin in presence of the different applied electric fields: (±) 0.01, (±) 0.05,(±)1.0 Vnm^{-1} and (±) 3.0 V nm^{-1}.

Steered molecular dynamics (SMD) simulations [22, 45] are executed on the average complex structure obtained from the 50 ns production simulation for 500 ps using a pull rate of 0.01 nm ps^{-1} and a force constant of 1000 kJ mol^{-1} nm^2. Here, the TBA is position restrained, the z axis is chosen as the reaction coordinate and the center of mass (COM) pulling technique is implemented, wherein the thrombin is pulled along the reaction co-ordinate. The free energy of binding ($\Delta G_{binding}$) between TBA and thrombin molecule is calculated using the umbrella sampling (US) technique and the WHAM (Weighted Histogram Analysis Method) algorithm[45-47]. 42 windows are selected for the umbrella sampling simulations from a series of configurations extracted from the trajectory of the SMD simulation. In each of these windows a short 100 ps NPT equilibration followed by a

10 ns umbrella sampling simulation under the NPT ensemble is undertaken for a total of 424.2 ns of umbrella sampling simulations. The results are incorporated into the WHAM framework to compute the potential of mean force (PMF) profile (more details provided in Appendix A).

SMD simulations for 500 ps are also performed under influence of (±) 1.0 V $nm^{-1}$and (±) 0.5 V nm^{-1} electric fields along the (+) *z* axis. Pull rates of 0.006 nm ps^{-1} and 0.008 nm ps^{-1} are respectively used for (+) 1.0 V nm^{-1} and (+) 0.5 V nm^{-1} cases to ensure full dissociation of the complex, while for all other simulations 0.01 nm ps^{-1} is sufficient. Each of the 5 ns electric field MD and 500 ps SMD simulations were conducted independently for 5 times to observe the average behavior of the system. Additional details on the MD simulations are included in Appendix A.

2.4 Results and discussion

Electric field inside the DNA layer

The electric field variation with distance from the electrode surface as obtained from the solutions of the PBE described in equation (3) are plotted in Figures 2(a) and (b) for grafting density $\sigma = 10^{12}$ cm^{-2} and 10^{11} cm^{-2} respectively.

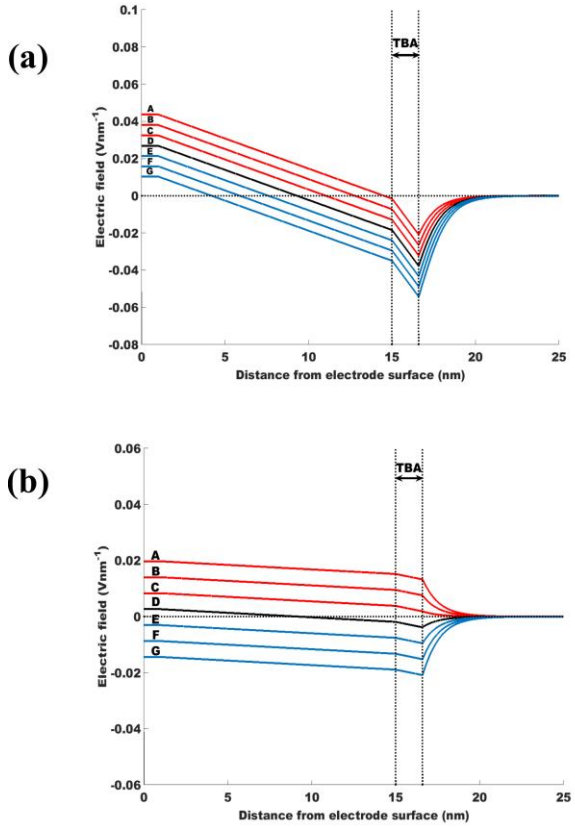

Figure 5: **The evolution of the electric field from the electrode surface is presented for the TBA in salt solution, where the DNA density (a) $\sigma = 10^{12}$ cm^{-2} and (b) $\sigma = 10^{11}$ cm^{-2}. Curves A, B, C, D, E, F and G respectively correspond to the electrode potential of +300 mV, +200 mV, +100 mV, 0 mV, -100 mV ,-200 mV and -300 mV .**

We observe from Figure 5(a) that initially the field is constant up to 1 nm from the electrode surface as this space is occupied by the neutral portion (thiol) of the linker. Further away, the

field varies linearly as the DNA charge is constant within the layer. The change in the field is more pronounced inside the region occupied by TBA G-quadruplex (between 15 and 16.6 nm) as evidenced by the steeper slope. Here, the occurrence of stronger charge density relative to the rest of the DNA molecule produces a significant change in electric field over a shorter distance. Outside the layer the field lines are nonlinear because of the hyperbolic charge density of the ions. We find from Figure 5(a) that the field inside the DNA layer becomes progressively positive with increasing positive electrode potentials. At an electrode potential of (+) 300 mV the field, inside the DNA layer, is predominantly positive relative to that for (-) 300 mV. Similar characteristics are observed for the electric field for a reduced DNA density in Figure 5(b), but the field is entirely positive over the whole domain for positive electrode potentials. Figure 5(a) also reveals that at $\sigma = 10^{12}$ cm^{-2} and for an electrode potential of (+) 300 mV, the electric field inside the DNA layer switches from positive to negative across the layer height through a change in magnitude of ~0.06 V nm^{-1}. In contrast, from Figure 5(b) it is found that for $\sigma = 10^{11}$ cm^{-2} , while the electric field remains positive inside the layer, there is a slight drop in the field strength across the layer thickness even if it is an order of magnitude lower at ~0.002 V nm^{-1}. Expectedly the more negative charges on account of the denser DNA layer produce enhanced shielding even when the electrode potential is substantially positive, thus explaining the greater drop in field strength for the higher grafting density. Hence, our results show that the electric field distribution in the negatively charged layer of DNA depends on the grafting density and applied surface potentials. For $\sigma = 10^{12}$ cm^{-2} , the electric field near the surface of the DNA layer, where the aptamer head containing the G-quadruplex is located, remains negative for the range of potentials investigated in this study. At the lower grafting density of $\sigma = 10^{11}$

cm^{-2}, the electric field across the aptamer head is entirely positive for all three of the positive potentials investigated in this study. So under suitable electrode potential and grafting density, the field generated by the negatively charged DNA layer can be turned to positive. Physiologically, thrombin is positively charged [12] and, hence, would be repelled by the positive electric field inside the DNA layer. Therefore, a positively charged molecule situated over a TBA layer at an electrode potential of (+) 300 mV will experience a repulsive force that is stronger compared to that at (+) 100 mV since the electric field becomes increasingly positive with increasing positive electrode potential. For a potential of (-) 300 mV, the magnitude of the field at the top of the DNA layer is more negative for $\sigma = 10^{12}$ cm^{-2} compared to that for $\sigma = 10^{11}$ cm^{-2}. In both cases, thrombin would be attracted towards the layer, as shown in earlier experiments [23]. One of the assumptions behind the continuum analysis is that the structure of the TBA is maintained on binding with thrombin which is based on observations that the G-quadraplex structure of TBA is stabilized on binding with thrombin protein24. Also folding of the 35-mer linker as it is condensed upon itself may be approximated by decreasing the aptamer layer height. Continuum calculations for grafting density of $\sigma = 10^{11}$ cm-2 as well as $\sigma = 10^{12}$ cm^{-2} show that decreasing the height of linker layer results in similar trend in dependence of electrical fields on applied potential as shown in Figures 2a and b. Decreasing the linker layer height makes the electrical field at the top of the layer increasingly positive (explained in detail in Appendix A). Hence, the electrical filed magnitudes plotted in Figure 5 correspond to lower approximation for the electrical fields. Thus we conclude that the strength of this positive field increases with an increase in the applied positive electrode potential, increased condensation of the linker portion of the aptamer strand and reduction of grafting density.

Effect of electric field on TBA/thrombin complex

We examine the thrombin structure under different electric fields by employing MD simulations. We find that higher electric fields exerted a notable influence on the secondary structure of the protein. Root mean square deviation (RMSD) of the atomic positions of a protein obtained from simulation trajectories can be utilized to understand the conformational changes due to MD simulations of the protein with respect to a reference structure of the same protein at an equilibrated state. Analyses of RMSD of the thrombin molecule for different electric field strengths is shown in Figure 6.

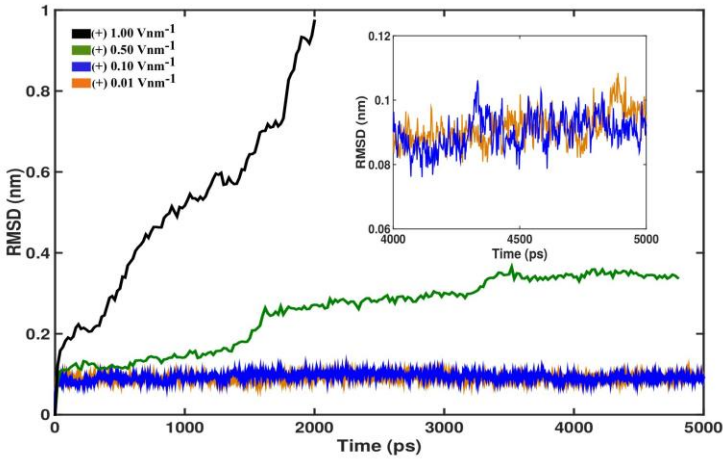

Figure 6: The transient evolution of thrombin RMSD for representative cases of electric field stimulus are shown as obtained from MD simulations. RMSD prediction is only for the time period when the thrombin is inside of the simulation box.

The reference structure is chosen from the average structure of the predominant cluster (84% occupancy in the 50 ns trajectory) in the 50 ns production run and a backbone least square fit is performed for the electric field simulations spanning 5 ns. The results, in Figure 6, show that for electric fields of (+) 0.01 and (+) 0.1 V nm^{-1} the structure is stable with an average RMSD value of around 0.085 nm. The inset shows the last 1 ns of the simulation for 0.01 and

0.1 Vnm^{-1}, where no deviations are noted from the average RMSD values. The RMSD curves for higher positive electric fields of (+) 0.5 and (+) 1.0 V nm^{-1} represent the dynamic behavior of thrombin structure. The RMSD for (+) 0.5 V nm^{-1} plateaus at ~0.32 nm after ~3500 ps (3.5 ns) of the simulation. We also note from Figure 3 that under the electric field of (+) 1.0 V nm^{-1}, the RMSD of thrombin increases very rapidly, indicating the stronger impact of the higher strength electric field on the protein structure and the thrombin molecule exits the simulation box within ~ 1.6 ns of the 5 ns simulation. Further analysis, on the thrombin structure under the influence of (+) 0.5 V nm^{-1}, shows that the protein shape is conserved well with respect to the structure at the start of simulation (discussed in detail in Appendix A). Interestingly, thrombin spontaneously dissociates from TBA at (+) 0.5 V nm^{-1}, in agreement with experimental findings that showed that the complex dissociated at an electrode potential of (+) 100 mV but remained bound at (-) 100 mV or the neutral condition (Figure 4(b)) [23]. This dissociation is not achieved under electric fields of (+) 0.01 and (+) 0.1 V nm^{-1} (Appendix A). From the continuum analysis discussed previously (Figure 5b), the top of the TBA layer is under an electric field of about (+) 0.006 V nm^{-1} and (+) 0.018 V nm^{-1} ,when the experimental electrode potential is (+) 100 mV and (+) 300 mV respectively. As in figures 18(i) and 18(j) (Appendix A), if we only consider the 15-mer aptamer for the continuum modeling of the experiments[23], then, at (+) 100 mV of electrode potential, for DNA grafting density of $\sigma = 10^{11}$ cm^{-2} and $\sigma = 10^{12}$ cm^{-2}, the electric field at the end of the layer is roughly 0.04 Vnm^{-1} and 0.03 Vnm^{-1} respectively. However, in the MD simulations dissociation is achieved at around 10 times (0.5 V nm^{-1} as compared to 0.04 V nm^{-1}) the electric field calculated in the continuum analysis. These differences can be attributed to the difference in time scales of the experiments, where the electrode potential is applied to the

complex over a few minutes to observe the dissociation, and the atomistic simulations run for only a few nanoseconds. Earlier reports have shown that the use of larger electric fields in MD computations with relatively much shorter simulation times produce results comparable to experiments [21, 25].

The dissociation of thrombin is again observed on application of (+) 1.0 V nm^{-1}, while for the simulations at (-) 0.1, (-) 0.5 and (-) 1.0 V nm^{-1}, there is no unbinding of the complex. Strong electric fields can distort the protein and compromise its functions. Thrombin structure deteriorates rapidly, wherein the protein is unfolded and stretched, within 1 ns of the 5 ns simulation for an electric field of (±) 3.0 V nm^{-1} (snapshots of the simulation available in Appendix A). It is observed that the thrombin remains bound with TBA even when the magnitude of the field is very strong and the protein structure is distorted. Earlier experiments have shown that application of voltages higher than (+) 300 mV can induce Faradaic currents on gold electrodes which in turn can denature DNA because pH changes can break gold-thiol bonds [26]. Thus, we conclude that successful modulation of the binding depends on the nature (positive/negative) as well as the magnitude of the electric field.

A hydrogen bond (H-bond) analysis for representative MD simulations is presented in Figure 7 The results imply a direct relation between electric field strength and H-bond formation. H-bonds cease to exist as the complex gets separated and the rate of decrease is directly proportional to the increasing positive electric field.

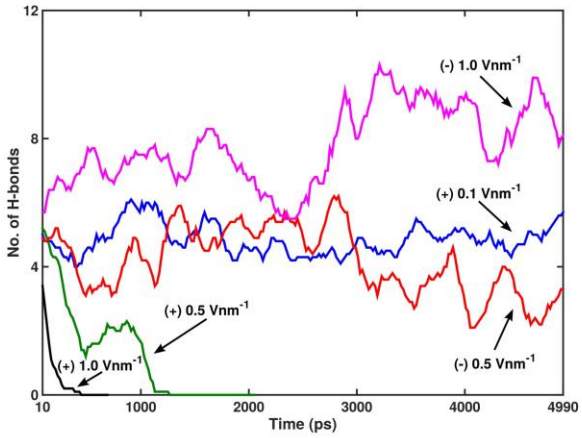

Figure 7: The H-bond population between TBA and thrombin for representative cases of electric field stimulus are shown as obtained from MD simulations. A running average over 10 data points is used for clarity of presentation

Under the electric fields of (+) 0.5 and (+) 1.0 V nm^{-1}, thrombin is dissociated from TBA and exits the simulation box at ~ 2157 ps and 790 ps, and H-bonds between the two molecules do not form beyond ~1220 ps and 390 ps, respectively. We determine the existence of an interaction between specific residues of the protein and the aptamer by analyzing the hydrophilic interactions, in terms of H-bonds, as well as the hydrophobic contacts between the protein amino acid side chains and the DNA bases. Previous efforts have shown that Arg-75 of thrombin forms hydrogen bonds with the T13 and T4 residues of the aptamer and Arg-77A interacts with T13 and G14 bases [17, 27]. These interactions are also observed in the simulations with positive electric fields, but their formations are notably reduced. Instead, the T4 base is found to interact with Arg-77A during the dissociation process. It is observed that both NH1 and NH2 atoms of Arg-77A donate a hydrogen to one of the carbonyl O atoms of the T4 base as thrombin gradually unbinds from TBA. An important interaction not present in the simulations with (+) 0.5 and (+) 1.0 V nm^{-1} is the H-bond between Tyr-76 and T4, as detailed in previous literature[17, 27], although it is observed for the smaller positive electric

field of (+) 0.1 V nm^{-1}. H-bond count at the start of simulation is relatively lower for the higher positive electric fields. We also note from Figure 4 that for the last 2000 ps of the simulation the average H-bond count is less for the (-) 0.5 V nm^{-1} field relative to that for the (+) 0.1 V nm^{-1}. Visual analysis of the simulation for (-) 0.5 V nm^{-1} reveals that thrombin is still bound to the TBA. Also the globular protein undergoes an overall angular movement wherein it is shifted along the *y*- axis of the simulation box. Further analysis shows that the exosite-I residues have limited avenues to interact with the TT loops of the aptamer, due to the reorientation of the protein. A new interaction between Lys-110 and T3 is observed; the NZ group donates hydrogen to the N3 and later to the O2 group of atoms in the T3 base of TBA, during the course of the simulation. As the electric field is increased to (-) 1.0 V nm^{-1} it is observed that the thrombin is pushed backwards (backward drift) along the + z axis towards the TBA. This facilitates additional interatomic interactions, which in turn results in a considerable increase in H-bond count when compared to that observed for other electric field simulations. The T3 base is observed to participate in H-bonding with Met-84, Arg-67, Lys-81 and Lys-110 residues of thrombin. Also prominent interactions are observed between Arg-73 and G6, Ser-72, Thr-74 and Arg-67 with G5, Arg-77A, Lys-109 and Arg-67 with G2. The interactions with the G-bases of the aptamer are enabled by the reorientation of the protein due to the backward drift under the negative electric field. Thus we find that under the negative electric fields the protein reorients with respect to the aptamer, newer interactions are promoted and the complex is still bound (Appendix A).

Insight from SMD simulations at (-) 1.0 V nm^{-1}

The results of the pulling simulation at (-) 1.0 V nm^{-1} are presented in Figure 8. Figures 8(a) and 8(b) show that complete dissociation of thrombin from TBA is not achieved

for pull rates of 0.008 and 0.01 nm ps^{-1} when using a harmonic force constant of 1000 kJ mol^{-1} nm^2. Even upon increasing the force constant to 12560.4 kJ mol^{-1} nm^2 (Figure 8(c)), as employed in the literature [22], we find that complete unbinding does not occur. Extensive discussions on the choice of the restraining potential and its influence on the predicted results are provided in the Appendix A. Experiments have demonstrated that at a negative electrode potential of (-) 300 mV there exists a pushing force which destroys the nanostructure of the complex upon the gold electrode [23]. H-bond analysis on the negative field SMD simulations prove that there is strong adherence of exosite-I residues to the TT loops as well as the G-quartet of TBA at (-) 1.0 V nm^{-1} even if a pull force is applied for breaking the bonds. As shown in figure 8(c), for the highest force constant as well as pull rate employed in our simulations, at (-) 1.0 V nm^{-1}, there is strong interaction between the TT loops of TBA and exosite-I residues of thrombin. While at longer simulation times the bonds will eventually break under the effect of the pull force, the protein does experience a pushing force (opposite to the pull direction) under negative electric fields.

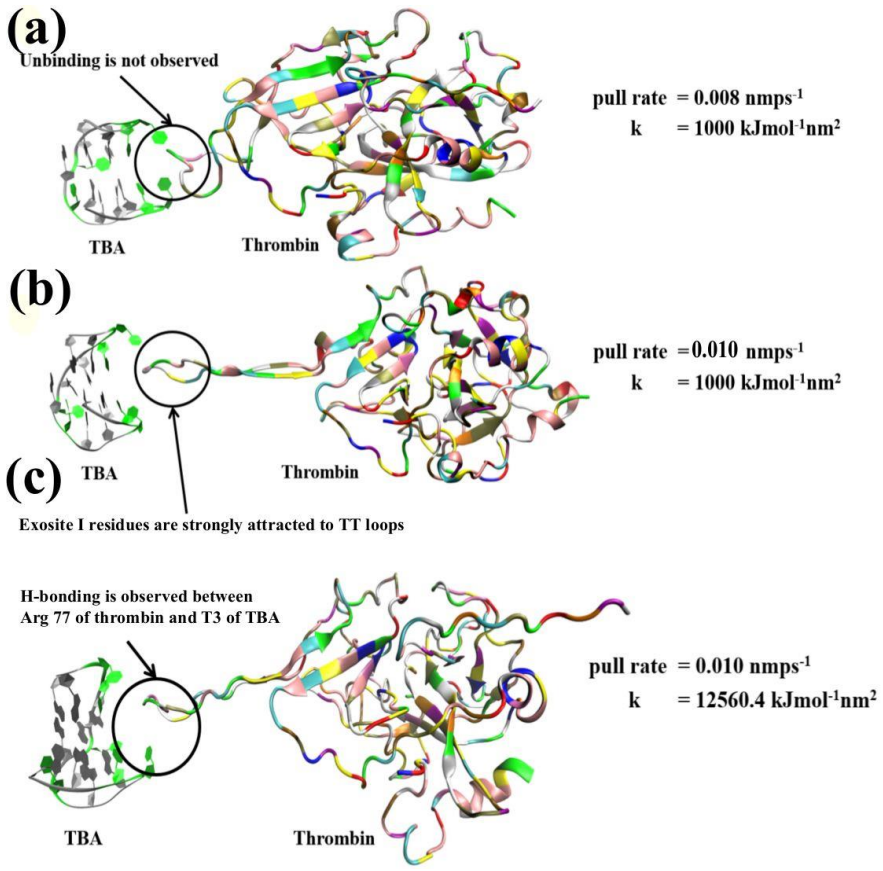

Figure 8: The binding between thrombin and TBA is shown, as observed in different SMD simulations, with varying force constants and pull rates, for the electric field of (–) 1.0 Vnm^{-1} and (a) pull rate = 0.008 nmps^{-1}, harmonic constant = 1000 kJmol^{-1}nm^2, (b) pull rate = 0.01 nmps^{-1}, harmonic constant = 1000 kJmol^{-1}nm^2, (c) pull rate = 0.01 nmps^{-1}, harmonic constant = 12560.4 kJmol^{-1}nm^2 .

As a result of this pushing force the thrombin experiences a backward drift i.e. opposite to the pull direction, towards the TBA, which in turn promotes the molecular interactions. This interpretation is supported by our results from the continuum analysis, as discussed above, that describes the electric field generated by the DNA layer at an electrode potential of (-) 300 mV to be primarily negative and affinity of the thrombin towards the TBA layer.

Free energy of binding from SMD and US simulations

Next, we calculate the free energy of binding between thrombin and TBA for specific electric fields of (+) 1.0 and (±) 0.5 V nm^{-1}. Atomic trajectories are generated from SMD computations for use in US simulations. As described above, on pulling the COM of the protein, force builds up until a breaking point is reached when the critical interactions are disrupted, allowing the thrombin to dissociate from the aptamer. The stretching of the imaginary spring attached to the COM of the thrombin, upon the breaking of bonds within the TBA/thrombin complex, gives rise to the force.

Figure 9(a) shows the evolution of this force with respect to the SMD simulation time for the (+) 0.5, (-) 0.5 and (+) 1.0 V nm^{-1} cases relative to that in absence of any electric field. For (+) 0.5 and (+) 1.0 V nm^{-1}, the maximum force values are small because the application of these electric fields spontaneously dissociates the thrombin. For the neutral case with no electric field, the maximum force is ~1080 kJ mol^{-1} nm^{1} occurring at 168 ps at a COM separation distance of ~1.67 nm. The last hydrogen bond between TBA and thrombin is recorded at 238 ps at a COM separation distance of ~2.41 nm. The maximum force for (+) 0.5 Vnm^{-1} is ~668 kJ mol^{-1} nm^{1} at 210 ps and for (+) 1.0 V nm^{-1} is 460 kJ$mol^{-1}$$nm^{1}$ at 117 ps, with the COM separation distances being 2.06 nm and 1.42 nm respectively. For (+) 0.5 V nm^{-1}, the last hydrogen bond within the TBA/thrombin complex is noted at 210 ps. At the higher electric field of (+) 1.0 V nm^{-1} the last hydrogen bond breaks at 218 ps when a COM separation is 2.01 nm, but a second maximum value of the force (435 kJ mol^{-1} nm^{1}) occurs at 289 ps. These results show that hydrogen bonding between thrombin and TBA ceases at lesser COM separation for increasing electric field. The reduction in H-bond formation

within the TBA/thrombin complex on application of positive electric fields has been discussed previously in this article.

The application of higher positive electric fields distorts the protein, promoting unfolding and

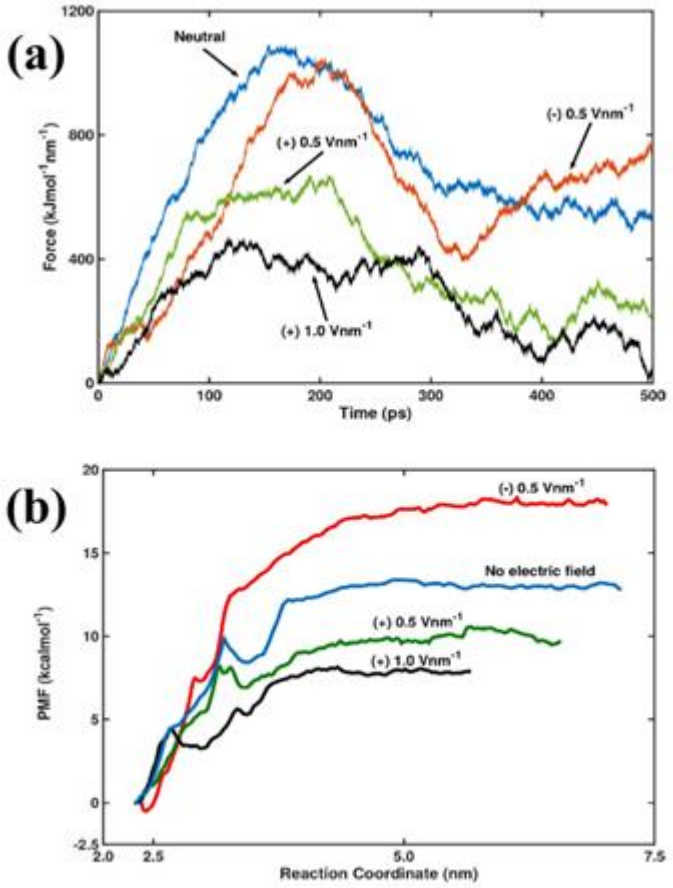

Figure 9: For representative cases of electric field stimulus in SMD simulations, the variation of (a) force (resulting from pulling the COM of thrombin) with time and (b) potential of mean force (PMF) evolution with reaction coordinate are presented.

this exposes the hydrophobic core and facilitates some amount of hydrophobic interactions with the ligand. Even when the H-bonding ceased between the TBA and thrombin, at (+) 1.0 V nm^{-1} , analysis revealed contacts between the hydrophobic residues Ile-82 and Ile-79 of exosite-I of thrombin and the T-3 and T-13 bases of TBA respectively. It may also be noted that there is absence of the gradual rise/decline of the force curve for the (+) 1.0 V nm^{-1} case

as compared to the other cases. The hydrophobic interactions stymied the sharp descent normally observed in the force curves of SMD simulations. After the second maximum force point, further analysis did not reveal any interaction between TBA and thrombin. In the case of (-) 0.5 V nm^{-1} potential, the maximum force value is ~1041 kJ mol^{-1} nm^{1} recorded at ~ 204 ps at a COM separation of 2.10 nm while the last hydrogen bond is observed at 241 ps for a COM separation of 2.57 nm. The maximum force value for the negative field is greater than that for the positive fields but less than that predicted for the neutral case.

Table 1 lists the free energy of binding ($\Delta G_{binding}$) values calculated from the PMF (Figure 9(b)) generated from the US simulations. We find that at (+) 0.5 and (+) 1.0 V nm^{-1}, $\Delta G_{binding}$ is significantly reduced. This facilitates the spontaneous dissociation of thrombin from TBA on application of positive electric fields. The $\Delta G_{binding}$ for the (-) 0.5 V nm^{-1} case is greater than that for the neutral case even though the maximum force is relatively less. As the last H-bond as well as the maximum force occurs later in the dissociation path for the negative field compared to the neutral case, we conjecture that increased bonded/non-bonded interactions between thrombin and TBA result in a higher binding energy.

Table 1: The comparison of free energy of binding for TBA/thrombin complex

Electric field (Vnm^{-1})	**0**	**(+) 0.5**	**(+) 1.0**	**(-) 0.5**
$\Delta G_{binding}$ (kcal mol^{-1})	**12.5 ± 0.9 ***	**8.5 ± 0.5**	**7.5± 0.7**	**17.5 ± 0.5**

*** The corresponding predictions for no electric field case from earlier computational and experimental investigations are 17 kcal mol^{-1} [22] and 9 kcal mol^{-1} [27] respectively.**

In all the COM pulling simulations, the point of maximum force corresponds to that instant when most of the bonds between the TT loop of the DNA and the interacting residues of exosite-I of thrombin are disrupted. The variations of the force on the COM of the thrombin with time derived from the SMD simulations are not sufficient to characterize the unbinding of TBA/-thrombin complex as this dissociation depends on the direction of pulling, choice of COM and the external applied potential. For a consistent COM definition and pulling direction, the dissociation depends on the events leading up to the separation between protein and DNA as well as the sign and magnitude of the electric field. If the dissociation path is similar, then a quantitative analysis of the unbinding of two molecules can be provided based on the transient evolution of the pull force. In all our SMD simulations the direction of pulling is always along the +*z* direction and this constrains the dissociation route. We find that for the positive fields the occurrence of maximum force (considering the 2^{nd} maximum for (+) 1.0 V nm^{-1} case as the 1^{st} and 2^{nd} maximum are close in value) is delayed in time relative to the neutral case. We attribute this to the slower pulling rates resulting in a prolonged dissociation event and lesser COM separation distance. This prediction is validated from the PMF profile in Figure 9(b), which shows that the reaction coordinate sampled is lesser for these electric fields. For the negative electric field, there is a backward drift (explained previously in the article) on the thrombin molecule that delays the occurrence of the maximum force compared to the neutral case. This backward drift causes an increase in the pull force on the thrombin at the end of the simulation after the drop in the force between 200 and 300 ps.

The electrostatic Coulombic and the Lennard-Jones (LJ) energies between the TBA and the thrombin molecules are monitored during the SMD simulations and are shown in

Figures 10(a) and 10(b) respectively. The Coulombic energy gives a measure of the extent of electrostatic interactions between the TBA and thrombin while the LJ energies quantify the dispersion/attractive as well as the repulsive/van der Waals interactions. From Figures 10(a) and 10(b) we find that both the Coulombic as well as the LJ interaction energy progressively increases for electric fields of (+) 1.0, (+) 0.5, 0 and (-) 0.5 V nm^{-1}.

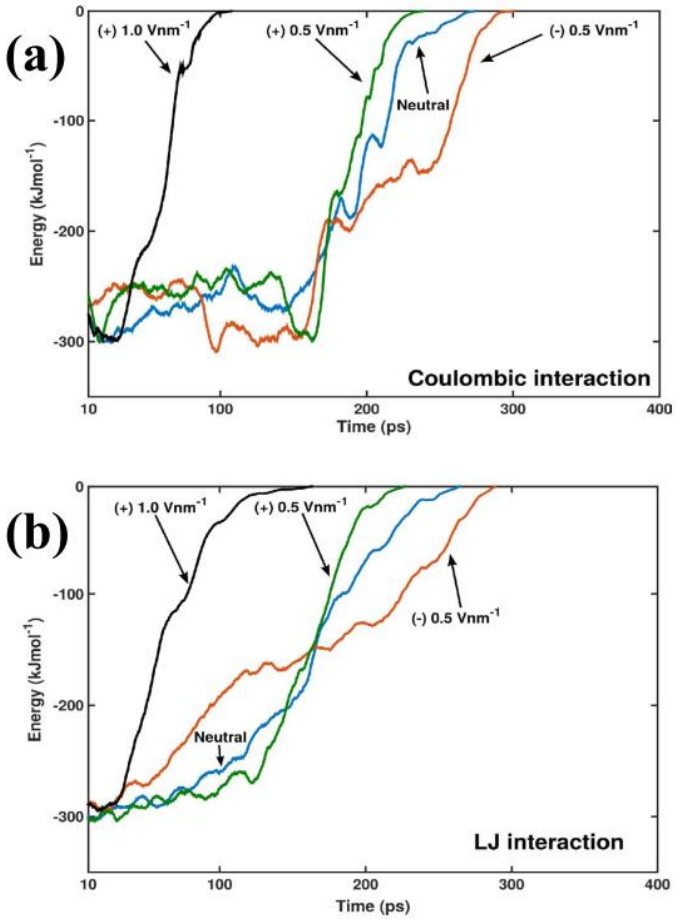

Figure 10: The transient evolution of the (a) electrostatic Coulombic and (b) potential energies due to non-bonded intermolecular interactions between the TBA and the thrombin molecules are shown for representative electric field SMD simulations.

We conclude that the higher positive electric fields decrease the interaction energy between TBA and thrombin resulting in lower $\Delta G_{binding}$. For the (+) 1.0 V nm^{-1} case, the increments

(from negative to zero) in both the Coulombic and LJ interaction energies are rapid, as noted by the steeper curves over a short time interval, relative to the (+) 0.5 Vnm^{-1} case. Consequently, $\Delta G_{binding}$ is smaller for (+) 1.0 than that for (+) 0.5 V nm^{-1}. On the other hand the electric field of (-) 0.5 V nm^{-1}, shows enhanced Coulombic interactions accompanied by higher LJ interaction energies. For the following representative electrical fields , (+) 1.0, (+) 0.5, 0 and (-) 0.5 V nm^{-1}, the total electrostatic Coulombic energies are -1.68, -4.82, -5.48 and -6.02 x 10^5 kJ mol^{-1} and the total LJ interaction energies are -1.84 , -4.53 , -4.68 and -4.97 x 10^5 kJ mol^{-1} respectively. Expectedly the negative field case has a higher PMF value compared to that of the neutral case.

2.5 Conclusion

We have employed a combination of continuum model and high-performance molecular computations to understand the role of external electrical stimulus on the binding and dissociation of thrombin-TBA complex. The simple, yet powerful, Poisson-Boltzmann theory based on a mean field model of the electrostatic interaction between particles reveals that at positive electrode potentials the DNA layer forms a repulsive region for the thrombin molecule, thereby acting as a deterrent to the complex formation. Predictions of the free energy of binding for the complex for different electric fields obtained from umbrella sampling simulations also suggest that for positive electric fields, the $\Delta G_{binding}$ is lesser compared to that of the neutral/negative case. The electrical stimulus influences the non-bonded interaction energies between thrombin and its aptamer as well as the H-bonding between the two; positive electric field reduces the non-bonded interaction energy and H-bonding between the TBA/aptamer complex which results in a reduced $\Delta G_{binding}$. In conjunction with earlier experiments, our molecular dynamics simulations of the

TBA/thrombin complex under positive electric fields show that the complex dissociates spontaneously and that the binding between protein-ligand complexes can be controlled through electrical stimulus. Our results open up an exciting avenue for potential biomedical applications involving DNA/protein complexes. The electrical field mediated modulation technique can be extended to processes involving targeted or controlled release of drug by application of external stimulus.

References

1. Wong, I.Y., Benjamin, A.D. & Melosh , N.A. Dynamic actuation using nano-bio interfaces. *Materials Today* **13**, 14-22 (2010).
2. Hianik, T., Ostatna, V., Sonlajtnerova, M. & Grman, I. Influence of ionic strength, pH and aptamer configuration for binding affinity to thrombin. *Bioelectrochemistry* **70**, 127-133 (2007).
3. Nguyen, T., Pei, R., Landry, D.W., Stojanovic, M.N. & Lin, Q. Label-free microfluidic characterization of temperature-dependent biomolecular interactions. *Biomicrofluidics* **5**, 34118-341187 (2011).
4. Willner, I. & Katz, E. Bioelectronics: From Theory to Applications Edited by Itamar Willner and Eugenii Katz. *Annals of Biomedical Engineering* **33**, 1464-1465 (2005).
5. Wong, I.Y., Footer , J.M. & Melosh, N.A. Electronically Activated Actin Protein Polymerization and Alignment. *J Am Chem Soc* **130**, 7908-7915 (2008).
6. Wong, K.Y. & Pettitt, B.M. Orientation of DNA on a surface from simulation. *Biopolymers* **73**, 570-578 (2004).
7. Wong, I.Y. & Melosh, N.A. An electrostatic model for DNA surface hybridization. *Biophysical journal* **98**, 2954-2963 (2010).
8. Rant, U. et al. Switchable DNA interfaces for the highly sensitive detection of label-free DNA targets. *Proceedings of the National Academy of Sciences of the United States of America* **104**, 17364-17369 (2007).
9. Rant, U. et al. Dynamic electrical switching of DNA layers on a metal surface. *Nano Letters* **4**, 2441-2445 (2004).
10. Ellington, D.A. & Sjostak, W.J. In vitro selection of RNA molecules that bind specific ligands. *Nature* **346**, 818-822 (1990).
11. Hermann, T. & Patel , J.D. Adaptive Recognition by Neuclic Acid Aptamers. *Science* **287**, 820-825 (2000).
12. Bode, W. et al. The refined 1.9 A crustal structure of human alpha-thrombin : interaction with D-Phe-Pro-Arg chloromethylketone and significance of the Tyr-Pro-Pro-trp insertion segment. *The EMBO Journal* **8**, 3467-3475 (1989).
13. Bock, C.L., Griffin, C.L., Latham, A.J., Vermass, H.E. & Toole , J.J. Selection of single stranded DNA molecules that bind and inhibit human thrombin. *Nature* **355** (1992).
14. Tasset, D.M., Kubik, M.F. & Steiner, W. Oligonucleotide inhibitors of human thrombin that bind distinct epitopes. *Journal of Molecular Biology* **272**, 688-698 (1997).
15. Russo Krauss, I. et al. Thrombin-aptamer recognition: a revealed ambiguity. *Nucleic acids research* **39**, 7858-7867 (2011).
16. Reshetnikov, R.V., Golovin, A.V. & Kopylov, A.M. Comparison of models of thrombin-binding 15-mer DNA aptamer by molecular dynamics simulation. *Biochemistry (Moscow)* **75**, 1017-1024 (2010).
17. Reshetnikov, R.V., Andrew, G., Vera, S., Alexei, K. & Jiri, S. Structural Dynamics of Thrombin-Binding DNA Aptamer d(GGTTGGTGTGGTTGG) Quadruplex DNA Studied by Large-Scale Explicit Solvent Simulations. *Journal of Chemical Theory and Computation* **6**, 3003-3014 (2010).

18. Marathias, V.M. & Bolton, P.H. Structures of the potassium-saturated, 2:1, and intermediate, 1:1, forms of a quadruplex DNA. *Nucleic acids research* **28**, 1969-1977 (2000).
19. Tsvetkov, V.B. et al. A Universal Base in a Specific Role: Tuning up a Thrombin Aptamer with 5-Nitroindole. *Scientific Reports* **5**, 16337 (2015).
20. Astrakas, L., Gousias, C. & Tzaphlidou, M. Electric field effects on chignolin conformation. *Journal of Applied Physics* **109**, 094702 (2011).
21. Wang, X., Li, Y., He, X., Chen, S. & Zhang, J.Z. Effect of strong electric field on the conformational integrity of insulin. *J Phys Chem A* **118**, 8942-8952 (2014).
22. Kim, E., Yang, C. & Pak, Y. Free-Energy Landscape of a Thrombin-Binding DNA Aptamer in Aqueous Environment. *Journal of Chemical Theory and Computation* **8**, 4845-4851 (2012).
23. Ma, Xiao, "Electrostatic actuation based modulation of polar molecules and associated force interaction studies" (2013). *Graduate Theses and Dissertations.* Paper**13488**. (http://lib.dr.iastate.edu/etd/13488).
24. Radi, A.-E., Acero Sánchez, J.L., Baldrich, E. & O'Sullivan, C.K. Reagentless, Reusable, Ultrasensitive Electrochemical Molecular Beacon Aptasensor. *Journal of the American Chemical Society* **128**, 117-124 (2006).
25. Benavidez, T.E., Torrente, D., Marucho, M. & Garcia, C.D. Adsorption of Soft and Hard Proteins onto OTCEs under the Influence of an External Electric Field. *Langmuir* **31**, 2455-2462 (2015).
26. Sosnowski, R.G., Tu, E., Butler, W.F., O'Connell, J.P. & Heller, M.J. Rapid determination of single base mismatch mutations in DNA hybrids by direct electric field control. *Proceedings of the National Academy of Sciences of the United States of America* **94**, 1119-1123 (1997).
27. Pagano, B., Martino, L., Randazzo, A. & Giancola, C. Stability and binding properties of a modified thrombin binding aptamer. *Biophysical journal* **94**, 562-569 (2008).
28. Yu, J., Jiang, Y., Ma, X., Lin, Y. & Fang, X. Energy Landscape of Aptamer/Protein Complexes Studied by Single-Molecule Force Spectroscopy. *Chemistry–An Asian Journal* **2**, 284-289 (2007).
29. Schultze, P., Macaya, R.F. & Feigon, J. Three-dimensional Solution Structure of the Thrombin-binding DNA Aptamer d(GGTTGGTGTGGTTGG). *Journal of Molecular Biology* **235**, 1532-1547 (1994).
30. Manning, G.S. Limiting Laws and Counterion Condensation in Polyelectrolyte Solutions I. Colligative Properties. *The Journal of Chemical Physics* **51**, 924 (1969).
31. Borukhov, I., Andelman, D. & Orland, H. Steric Effects in Electrolytes: A Modified Poisson-Boltzmann Equation. *Physical Review Letters* **79**, 435-438 (1997).
32. Stachowiak, J.C., Yue, M., Castelino, K., Chakraborty, A. & Majumdar, A. Chemomechanics of Surface Stresses Induced by DNA Hybridization. *Langmuir* **22**, 263-268 (2006).
33. Padmanabhan, K. & Tulinsky, A. An Ambiguous Structure of a DNA 15-mer Thrombin Complex. *Acta Crystallographica Section D* **52**, 272-282 (1996).
34. Hornak, V. et al. Comparison of multiple Amber force fields and development of improved protein backbone parameters. *Proteins: Structure, Function, and Bioinformatics* **65**, 712-725 (2006).

35. Perez, A. et al. Refinement of the AMBER force field for nucleic acids: improving the description of alpha/gamma conformers. *Biophysical journal* **92**, 3817-3829 (2007).
36. Berendsen, H.J.C., Spoel, D.v.d. & Drunen, R.v. GROMACS: A message-passing parallel molecular dynamics implementation. *Computer Physics Communication* **91**, 43-56 (1995).
37. Ahmed, H.U. et al. The determination of protonation states in proteins. *Acta Crystallographica Section D* **63**, 906-922 (2007).
38. Jorgensen, W.L., Chandrasekhar, J., Madura, J.D., Impey, R.W. & Klein, M.L. Comparison of simple potential functions for simulating liquid water. *The Journal of Chemical Physics* **79**, 926 (1983).
39. Bussi, G., Donadio, D. & Parrinello, M. Canonical sampling through velocity rescaling. *J Chem Phys* **126**, 014101 (2007).
40. Berendsen, H.J.C., Postma, J.P.M., van Gunsteren, W.F., DiNola, A. & Haak, J.R. Molecular dynamics with coupling to an external bath. *The Journal of Chemical Physics* **81**, 3684 (1984).
41. Nosé, S. A unified formulation of the constant temperature molecular dynamics methods. *The Journal of Chemical Physics* **81**, 511 (1984).
42. Hoover, W. Canonical dynamics: Equilibrium phase-space distributions. *Physical Review A* **31**, 1695-1697 (1985).
43. Hess, B., Bekker, H., Berendsen, H.J.C. & Fraaije, J.G.E.M. LINCS : A linear constraint solver for molecular simulations. *Journal of computational Chemistry* **18**, 1463-1472 (1997).
44. Darden, T., Perera , L., Leping, L. & Pedersen, L. New tricks for modelers from the crystallography toolkit: the particle mesh Ewald algorithm and its use in nucleic acid simulations. *Structure* **7**, 55-60 (1999).
45. Lemkul, J.A. & Bevan, D.R. Assessing the stability of protofibrils using molecular dynamics. *Journal of Physical Chemistry B* **114**, 1652-1660 (2010).
46. Torrie, G.M. & Valleau, J.P. Nonphysical sampling distribution in Monte Carlo free energy estimation: umbrella sampling. *Journal of Computational Physics* **23**, 187-199 (1977).
47. Hub, J.S., Groot, B.L.D. & Spoel, D.V.D. g_wham-A Free Weighted Histogram Analysis Implementation Including Robust Error and Autocorrelation Estimates. *Journal of Chemical Theory and Computation* **6**, 3713-3720 (2010).
48. Humphrey, W., Dalke, A. & Schulten, K. VMD: Visual molecular dynamics. *Journal of Molecular Graphics* **14**, 33-38 (1996).

CHAPTER 3. FORCE SPECRTROSCOPY OF THE THROMBIN-APTAMER INTERACTION: COMPARISON OF ATOMIC FROCE MICROSCOPE BASED MEASUREMENTS AND MOELCULAR DYNAMICS SIMULATIONS

Xiao Ma[1], Janice Marquardt[1], Agnivo Gosai[1,a], Marit Nilsen-Hamilton[2], Ganesh Balasubramanian[1] and Pranav Shrotriya[*,2]

Modified from a paper to be submitted to *Langmuir*

3.1 Abstract

Force spectroscopy is used to characterize the bond strength and binding energy between thrombin and its single-stranded DNA aptamer. Atomic force microscope (AFM) based experiments are conducted on the thrombin/aptamer and other non-specific binding systems to ensure that the measured binding forces are specific to the dissociation of the thrombin/aptamer complex. A thrombin-coated AFM tip is first brought into contact with the receptor-functionalized surface and subsequently retracted from the surface at a controlled displacement rate. The force response associated with probe retraction is analyzed to determine the force and loading rate associated with dissociation of the protein/receptor complex. Experimental results show that force curves have the characteristic sequential unbinding response and larger dissociation forces only for the combination of thrombin and the specific binding receptor (thrombin aptamer). The distribution of forces measured for different loading rates on the thrombin aptamer coated surface are analyzed to provide

[a] Author of this thesis ; carried out the computational work described in this chapter
[1] Department of Mechanical Engineering, Iowa State University, Ames, IA 50010
[2] Department of Biochemistry, Biophysics, and Molecular Biology, Iowa State University, Ames, IA 50010
[*] To whom correspondence should be addressed, Email: shrotriy@iastate.edu

estimates of the dissociation force as a function of loading rate associated with thrombin/aptamer complex, and show that the dissociation force increased from 20 pN to 40 pN as the loading rate is increased from 100 pN/s to 40000 pN/s. The measured dissociation force magnitudes for the thrombin/aptamer unbinding are lower than forces associated with G-quadruplex unbinding and comparable to forces associated with DNA unfolding Steered molecular dynamics simulations are utilized to model the thrombin and aptamer unbinding to estimate the dissociation forces over loading rates ranging from 0.001 N/s to 10 N/s. Availability of computational resources limits simulations only to loading rates significantly faster than experimental observations but comparison of the measured and predicted response shows that both dissociation force show similar dependence on loading rates.

3.2 Introduction

Dynamic Force Spectroscopy (DFS) has been utilized to measure dissociation forces between specific complementary chemical and biological molecules [1-3]. Analysis of the unbinding forces reveals remarkable insight into energy consumption, binding kinetics and thermodynamic parameters for the molecular bonds [4]. These advantages make it a useful tool for probing the nature and mechanism of biomolecular interactions and cellular adhesion. However, DFS experiments are limited to slow loading rates. Molecular dynamics simulations may be used to simulate the unbinding response but constraints in computational resources limit the simulations to orders of magnitudes faster than experimental conditions. We report comparison between experimental and computational DFS-based analysis of the specific binding between thrombin and its DNA aptamer in order to characterize the DFS response over a significantly larger loading rate than previously reported.

Aptamers are engineered nucleic acids that are selected from a random pool using the "systematic evolution of ligands by exponential enrichment" (SELEX) procedure [5-7], to have a high specific binding affinity towards a target biomolecule [8-13]. Aptamers display similar specific affinity for their target analyte as antibodies and have the following additional advantages over antibodies for application to analytical platforms: stable over a larger range of temperatures and conditions; easily regenerated and reused; and easily modified or functionalized for different applications. Thrombin catalyzes the synthesis of fibrin from fibrinogen so as to facilitate coagulation during blood clotting. Two DNA aptamers have been selected for binding specifically with thrombin at different binding sites – Aptamer 1 (15apt – GCCTTAACTGTAGTACTGGTGAAATTGCTGCCATT**GGTTGGTGTGGTTGG** [14-18]) and Aptamer 2 (27apt – CTTTGGAGACA**GTCCGTGGTAGGGCAGGTTGGGGTGAC** TTCGTGGAAGAAGCGAGACGGT [16, 18]) The aptamer (15apt) used in this study was selected by Bock et al. [15] and contains the 15 nucleotide consensus sequence d(GGTTGGTGTGGTTGG) that forms a G-quadruplex [15, 18-20] and binds to thrombin's fibrinogen binding site [18, 21]. This aptamer has been shown in chemical assays to have high binding specificity to thrombin with a dissociation constant (K_d) of 1 to 6 nM [20, 22]. The strength of the interaction between thrombin and its aptamer makes it relevant for the study of binding forces and suitable for a force spectroscopy study.

Previous reports on DFS based measurements of the dissociation forces between this aptamer (15 apt) and thrombin have shown little agreement [14, 23, 24]. Basnar et al. [14] utilized atomic force microscope to study the disruption of the binding complex at a loading rate of 3000pN/s. The force quantum associated with dissociation of the complex was calculated to be 4.45 pN by taking the peaks from the force distribution histogram and performing linear

regression. The magnitude of the reported force quantum is surprisingly close to the thermal force level and is significantly lower than the force magnitude of stable bond strengths reported for a G-quadruplex interacting with specific binding partners. Yu et al. [23] reported dissociation force varying in range of 60-100 pN over an apparent loading rate varying from 12000 pN/s to 2×10^5 pN/s and in the range of 90 – 250 pN over a loading range of 2×10^5 pN/s to 1.7×10^6 pN/s. Neundlinger et al. [24] immobilized single biotinylated stabilized thrombin aptamer molecule on the AFM tip and measured dissociation forces of 50 pN to 150 pN over a loading range of 500 pN/s to 20,000 pN/s.

Miyachi et al. [25] developed an AFM-SELEX cycle to select stronger affinitive DNA aptamer to thrombin under a very high loading rate level (~ 10^5 pN/s), and acquired much higher affinity force between a different aptamer sequence and thrombin. Ge, et al. [16] investigated the binding interaction via dynamic force spectroscopy between thrombin and a bivalent DNA aptamer which contains thrombin's two aptamers (15apt and 27apt) linked by eight spacer phosphoramidites, and showed that the dissociation force ranged from 60 to 150 pN under loading rates from 2000 pN/s to 5×10^5 pN/s.

Lynch et al. [26] used AFM to investigate the dissociation behavior of G-quadruplex DNA composed of 3 and 4 G tetrads, and found the most likely unbinding forces for disruption of both the 3G and 4G quadruplex structure to be from 40 to 70 pN, corresponding to loading rates from 1000 pN/s to 50000 pN/s. Pope et al. [27] used AFM to study the melting of double strand DNA and obtained the most likely unbinding forces for unzipping a 12-mer double helical DNA to be from 23 to 40 pN, which correspond to loading rates from 100 pN/s to 6000 pN/s. Using a biomembrane force probe, Erdmann et al. [28] measured the force

magnitude associated with dissociation of biotin-streptavidin bonds to be from 50 to 80 pN, corresponding to loading rates from 100 pN/s to 10000 pN/s.

The significant difference between force magnitudes reported for thrombin/aptamer binding (4.45 pN to 200 pN) and other other binding complexes (23 - 80 pN) indicates a need for closer evaluation of the thrombin/aptamer binding interactions. Here we utilize experiments and computational approaches to report the dissociation force for the thrombin/aptamer complex over a significantly larger range of loading rates. The measured unbinding forces are compared to other binding complexes to suggest a mechanism underlying the dissociation process. The dissociation forces are also analyzed using a single energy barrier model to estimate the magnitude of spontaneous dissociation time and energy barrier width for the thrombin/aptamer interaction.

3.3 Experimental Characterization

Binding forces were measured between a thrombin-coated AFM tip and three different surfaces that were functionalized with either thiolated poly(ethylene)glycol (PEG, 2 kDa) or 5' thiolated single stranded poly(dA) (pHS-A_{30}), or 5' thiolated 50nt-thrombin aptamers (HS-alkane-GCCTTAACTGTAGTACTGGTGAAATTGCTGCCATT**GGTTGGTGTGGTTGG**) [14, 15, 17, 18]. The force interaction with PEG surface was used to verify that the surface of tip was functionalized with proteins. Binding forces between thrombin aptamer and single stranded DNA (poly(dA)) were used to determine the magnitude of non-specific interactions. The interactions between thrombin and thrombin aptamer were investigated to determine the forces associated with specific binding.

All chemicals required for the experiments except PEG were purchased from Sigma Aldrich (www.sigma.com), and all oligonucelotides were purchased from Integrated DNA Technologies (www.idtdna.com). Poly(ethylene)glycol was purchased from Creative PEGworks (www.creativepegworks.com). All solutions were prepared with double distilled water (ddH_2O).

Atomic force microscope tips were coated with thrombin to measure the protein surface interactions. To functionalize the AFM tip, gold-coated silicon nitride tips were purchased from Novascan Technologies Inc. (www.novascan.com). The spring constant of each AFM tip was determined using Sader's method prior to functionalization [29]. Thrombin was immobilized on the gold coated AFM tip as follows: The probe was incubated first in 2 mM mercaptohexadecanoic acid (MHA) for 1 h to form a carboxyl-terminated self-assembled monolayer (SAM) on the gold surface, then in freshly prepared 10 mg/ml carbodiimide (EDAC) in ddH_2O for 30 min to activate the carboxylic acid groups for protein attachment to the AFM probe. The probe was then immersed in 1 mg/ml human thrombin in buffered saline solution (137 mM NaCl, 2.7 mM KCl, 10 mM Na_2HPO_4, 5 mM KH_2PO_4 in ddH_2O at pH 7.4 as adjusted with HCl) for 90 min to immobilize the protein on the activated carboxylic acid-terminated SAM surface. Last, the probe was washed 3 times for 5 min each in buffered saline solution and 3 times for 5 min each in ddH_2O. The probe was either used immediately or stored for less than 24 h in ddH_2O before use. A single AFM tip was used to collect at the most 200 force curves and a total of 25 different AFM tips were used for the experiments reported here.

The three functionalized surfaces - PEG, poly(dA) and thrombin aptamer- were prepared by attaching the molecules to a gold-coated silicon wafer through gold/thiol bond. A template

transfer technique was used to form a smooth gold film on the polished silicon wafers. To form the PEG functionalized surface, the gold-coated silicon wafers were incubated in thiolated PEG (1 mg/mL in ethanol) for 1 min. The poly(dA)-functionalized surfaces were prepared by immersion of the gold-coated wafer in 1 mg/ml thiolated poly(dA) in binding buffer (20 mM Tris-HCl, 140 mM NaCl, 5 mM KCl, 1 mM $CaCl_2$, 5 mM $MgCl_2$, and 5% glycerol (v/v) in ddH_2O at pH 7.4) for 1 min [14]. Finally, the thrombin-functionalized surfaces were prepared by immersion of the gold coated silicon wafers in 1 mg/ml thiolated aptamer in binding buffer. All functionalized surfaces were rinsed several times with ddH_2O and grounded with copper tape before being used for the unbinding experiments.

Force curve experiments for all coated substrates were performed in binding buffer using a Dimension 3100 atomic force microscope. During the experiments, the AFM tip was moved towards the sample to establish contact with surface and then retracted back to its starting location at a fixed displacement rate. The force applied to the AFM tip during surface contact and retraction was measured to obtain the force curves. The experimental study was conducted in two steps:

1) Force curves were acquired for the following functionalized surface/probe pairings - Polyethylene glycol coated surface/ thrombin coated probe (minimal binding); Poly(dA) coated surface/thrombin coated probe (non-specific binding); Aptamer coated surface/ mercaptohexadecanoic acid (MHA) coated probe (non-specific binding); and Aptamer coated surface/ thrombin coated probe (specific binding) – in order to compare unbinding force responses for specific and non-specific interactions.

2) Force curves were acquired to investigate the loading rate dependence of the force interaction associated with a specific binding event. In the initial step, force curves were obtained at a nominal displacement rate of 200 nm/s.

For each pairing, force curves were measured ten times per location, at 5 locations on 5 different samples, resulting in a total of 250 force curves. In the second stage, force curves were collected only on thrombin aptamer functionalized surface/thrombin coated tips at two different nominal displacement rates: 200 nm/s and 2000 nm/s. A total of two thousand force curves (10 samples X 20 locations/samples X 10 force curve/locations) were acquired for each displacement rate.

3.4 Computational Simulations

The crystallographic structure of TBA/thrombin complex (PDB entry 1HAO)] [30] was parameterized using the AMBER99SB force field [31] with parmbsc0 parameters [32] and the TIP3P water model [33] following previously published literature [34, 35] for molecular dynamics (MD) simulations using GROMACS 4.6.7 [36]. The biomolecular complex was solvated in a rectangular simulation box of dimensions 7.5 nm x 7.5 nm x 15 nm (*x* x *y* x *z*) with 26010 water molecules. 11 Na+ atoms are added to the solution to neutralize the system. Additionally, 51 Na+ atoms and 51 Cl^- atoms were randomly added to the system to build up a concentration of 0.1 M. Energy minimization was performed using the steepest descent algorithm, and the system attained a minimum energy configuration for a maximum force tolerance value of 500 $kJmol^{-1}nm^{-1}$. Next, the thrombin and aptamer atoms were position restrained and the system was equilibrated at 300 K and 1 bar with a time step of 2 fs (femtosecond) under (I) the canonical ensemble (NVT) using velocity rescaling thermostat [37] with coupling time constant of 0.1 ps (picosecond) for 1 ns (nanosecond), followed by (II)

another 1 ns simulation under the isothermal-isobaric ensemble (NPT) using the Berendsen barostat [38] with coupling constant of 5.0 ps and the previously mentioned thermostat. Initial atomic velocities were generated from a Maxwell distribution at 300 K before the equilibration process. On attaining target temperature and pressure, all position restraints were removed and MD simulations were performed under the NPT ensemble for 50 ns employing the Nose-Hoover thermostat [39, 40] with a coupling constant of 0.5 ps and the Parinello-Rahman [41] barostat with coupling constant of 1.0 ps.

The dynamical pulling simulations were performed on the complex structure obtained at the end of the 50 ns run which showed very low backbone C_α RMSD of 0.085 nm with respect to the crystallographic structure. The TBA was position restrained by applying a harmonic restraint of 1000 $kJmol^{-}1nm^{-2}$ to each of its atoms while the thrombin was pulled away from the binding mode of the complex by applying a harmonic force to the center of mass (COM) of the protein. This computational experiment, popularly referred to as Steered Molecular Dynamics (SMD) simulation [42], is fundamentally similar to the AFM method. We vary the pull rates between 0.0001 $nmps^{-1}$ to 0.0150 $nmps^{-1}$ maintaining the harmonic constant fixed at 1000 $kJmol^{-1}nm^{2}$ to understand the contribution of a range of forces on the structural evolution and unbinding of thrombin. The pulling direction is along the length of the box and chosen to be the +z axis. Alternately, the force constants can be varied by keeping the pull rate fixed, but earlier reports have shown that both the strategies reproduce qualitatively similar results [43]. The choice of the force constant is based on a different computational investigation by the authors for the same complex.

3.5 Experimental Results and Analysis

Representative force curves corresponding to interactions between the thrombin coated AFM tip and PEG and poly(dA) functionalized surfaces, and are shown in figures 1(a) and (b), respectively. Representative force curves corresponding to interaction between MHA coated AFM probe and thrombin aptamer functionalized surface are shown in figure 1 (c). Representative force curves corresponding to interactions between thrombin coated probe and aptamer functionalized surface representing sequential unbinding and single unbinding are shown in figures 1(d) and (e), respectively.

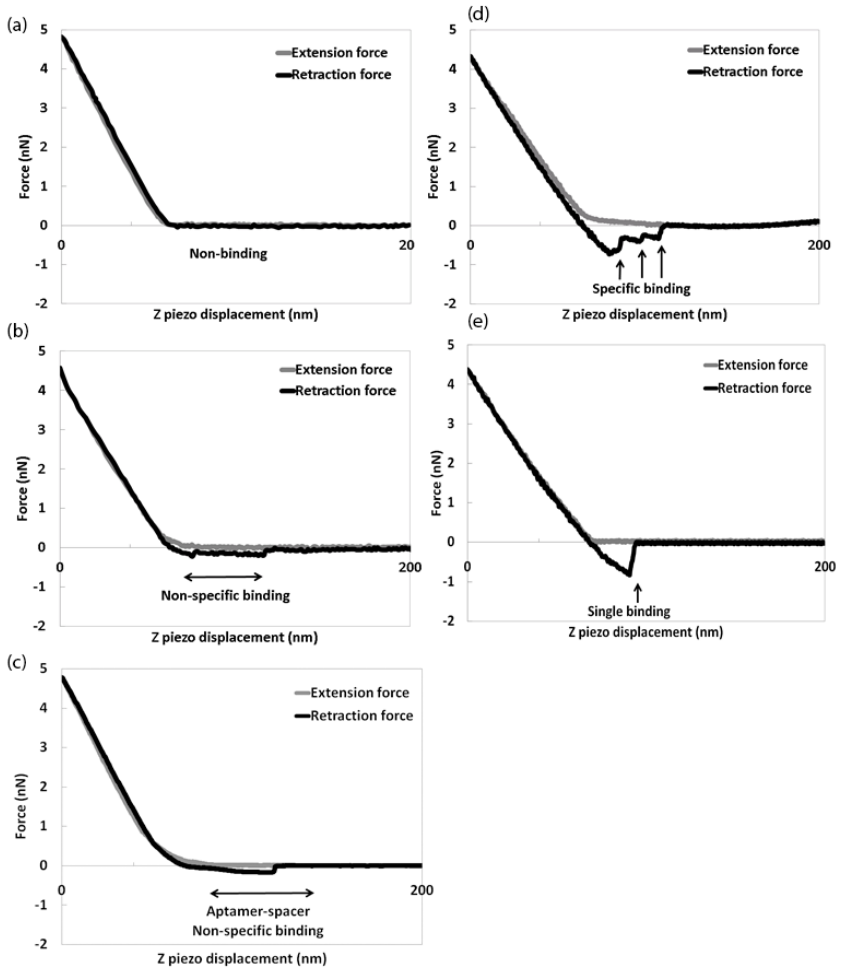

Figure 11 Representative force curves for functionalized AFM probe interacting with the different functionalized surfaces: (a) Thrombin coated probe vs PEG coated substrate; (b) Thrombin coated probe vs poly(dA) coated substrate); (c) MHA coated probe vs aptamer coated substrate; (d) Thrombin coated probe vs aptamer coated substrate(sequential unbinding) (e) Thrombin coated probe vs aptamer coated substrate(single unbinding).

For each functionalized surface, the force curves were collected on five different samples, and five locations per samples. The spring constant of each AFM tip was determined using Sader's method prior to functionalization and found to be within 0.06 ± 0.005 N/m for all the tips used in this study. The spring constants for the tips were used to determine the force displacement response plotted in figures 11(a), (b), (c), (d) and (e). We did not observe a systematic influence of these parameters on the measured force curves.

The force curves of the thrombin coated AFM tip against the PEG functionalized surface (shown in figure 1(a)) did not show any difference between the extension and retraction of the tip. This indicates that the AFM tip did not form any bonds with PEG functionalized surface, which is consistent with the generally observed lack of interaction between PEG and proteins [44-46]. Force curves in both thrombin coated probe/poly(dA) surface and MHA coated probe/ aptamer coated surface showed binding interactions. However, the retraction curves did not show obvious discrete drops in forces but rather an elongated displacement that ended with a small magnitude of force drop (labeled as non-specific binding events in figures 1b and c). The force curves of thrombin coated probe on the thrombin aptamer functionalized surfaces included either multiple discrete stepwise drops (labeled as specific binding events in figure 1d) or a single large drop (shown in figure 11e) of force in the retraction curve.

Discrete drops in forces have been suggested to be associated with sequential unbinding interactions between multiple bonds loaded in parallel [27, 28]. A comparison of these experimental observations indicates the following: 1) The difference in interactions of the thrombin-coated AFM tip with the PEG and aptamer functionalized surfaces shows that the tip was functionalized with protein molecules; (2) Binding between the protein and poly(dA) as well as MHA and thrombin aptamer requires low magnitude forces for dissociation; (3) Binding between the protein and aptamer requires a larger magnitude of forces and the retraction curve shows characteristics that are associated with dissociation of specific binding [27].

In order to determine the dependence of the unbinding forces on the loading rates, the force curves on the aptamer-functionalized surfaces were collected at two different displacement rates of the AFM cantilever (200 nm/s and 2000 nm/s). A total of over 4000 force curves (~2000 corresponding to each displacement rate) were collected and could be divided into three groups – no binding event was observed in approximately 15% of the force curves (601 out of 4031), single binding event (as shown in figure 11e) was observed in approximately 74% of the force curves (2978 out of 4031) and multiple binding events (as shown in figure 1d) were observed for approximately 11% of the force curves (452 out of 4031). Both thrombin on the probe surface and thrombin aptamer on the functionalized surface do not form a closely packed films, consequently some of the force curves do not show any binding, but at the same location other replication of the curves show either single or multiple binding events. The distributions of non-binding, single binding and multiple binding in the force curves agrees well with previously reported observations in other force spectroscopy experiments [27].

The dissociation forces and corresponding loading rates were determined from the retraction portion of force curves with multiple binding events as shown schematically in Figure 12, in order to determine the loading rate dependence of the dissociation force associated with specific binding. During the dissociation experiment, thrombin and aptamer were pulled apart at a constant displacement rate using the flexible atomic force cantilever. It is difficult to *a-priori* impose a desired loading rate during tip retraction. Instead, deformation of the AFM cantilever was used to determine the forces on the tip, and the loading rate can be determined as a product of applied displacement rate and the AFM cantilever stiffness only when the tip interacts with a rigid surface as indicated by the nominal loading rate in figure 12. Prior to the final unbinding, the imposed displacement is distributed between the AFM cantilever bending and deformation of protein/aptamer complexes. Hence the loading rate corresponding to the final dissociation is determined from the slope of the force curve just prior to the last unbinding event as indicated by the loading rate for unbinding in figure 12.

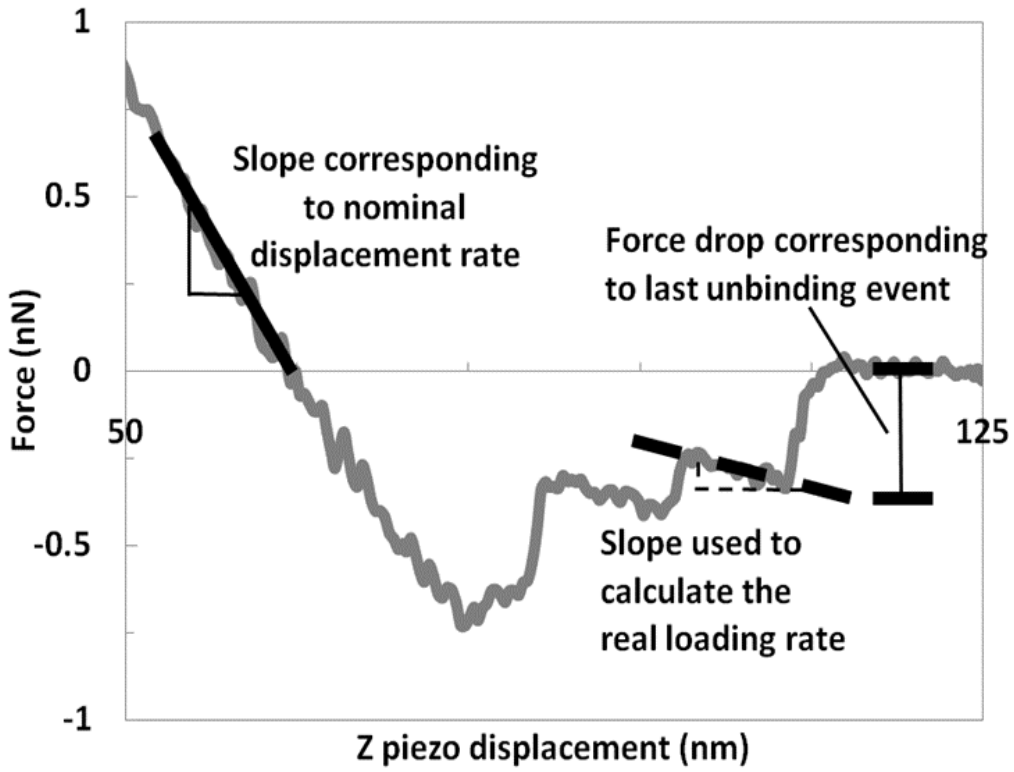

Figure 12 Representative force curve to demonstrate the computation of real loading rate using the loading information prior to final unbinding. The nominal and real loading rate are also indicated to highlight the difference between the two loading rates.

The dissociation force corresponding to the final dissociation event was determined from the load drop as shown in figure 2. The loading rate and dissociation force pairs were computed for each force curve that showed multiple binding events during the retraction. Only the last unbinding event of the multiple discrete force steps was used for analysis, as this last event is likely to have the fewest number of interacting bonds.

The dissociation forces determined from the force curves were found to be clustered into four groups based on the measured loading rate for the last unbinding event – lowest loading rate

(mean 90 pN/s and range 50 -140 pN/s); lower median loading rate (mean 750 pN/s and range 450 - 1200 pN/s); higher median loading rates (mean 7000 pN/s and range 4700 - 9500 pN/s) and highest loading rate (45000 pN/s and range 25700 - 63900 pN/s). The two lower loading rates were found primarily in the lower nominal displacement rate while the two higher loading rate clusters corresponded to higher displacement loading rate.

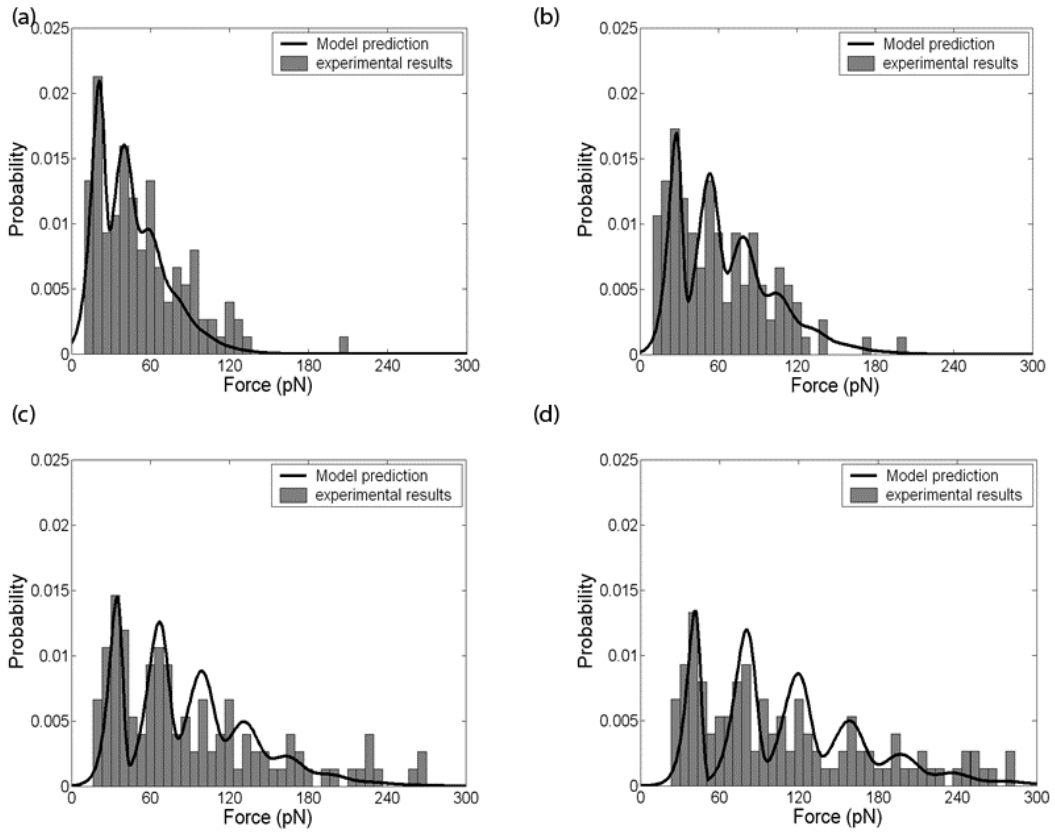

Figure 13 Experimentally measured distribution and comparison with predicted distribution of rupture forces for the thrombin-aptamer complex at different loading rates imposed prior to final unbinding event: (a) Lowest real loading rate (Average loading rate 90 pN/s); (b) Lower median real loading rate (Average loading rate 750 pN/s); (c) Higher median real loading rate (Average loading rate 7000 pN/s); and (d) Highest real loading rate (Average loading rate 45000 pN/s).

Distributions of the measured dissociation forces corresponding to specific binding at different loading rate levels – lowest, lower median, higher median and highest - are shown in figures 13(a), (b), (c) and (d), respectively. As the loading rates were increased, the range of the dissociation forces increased and the peaks in the probability distribution, which identify the most frequent force magnitudes, shifted towards higher magnitudes. A histogram of final load drop levels measured for a non-specific binding complex (poly(dA) and thrombin) is also plotted in figure 14 to compare the distributions corresponding to specific and non-specific binding. The comparison of the two distributions show the differences in magnitude of the measured forces for specific binding (thrombin-aptamer) and nonspecific binding (thrombin-poly(dA)). For the thrombin-aptamer complex, the distribution of rupture forces shows periodic peaks, which may indicate the existence of an elementary binding force corresponding to dissociation of a single protein/aptamer complex. In the case of thrombin-poly(dA) interaction, there are no obvious periodic peaks in the histogram of rupture forces.

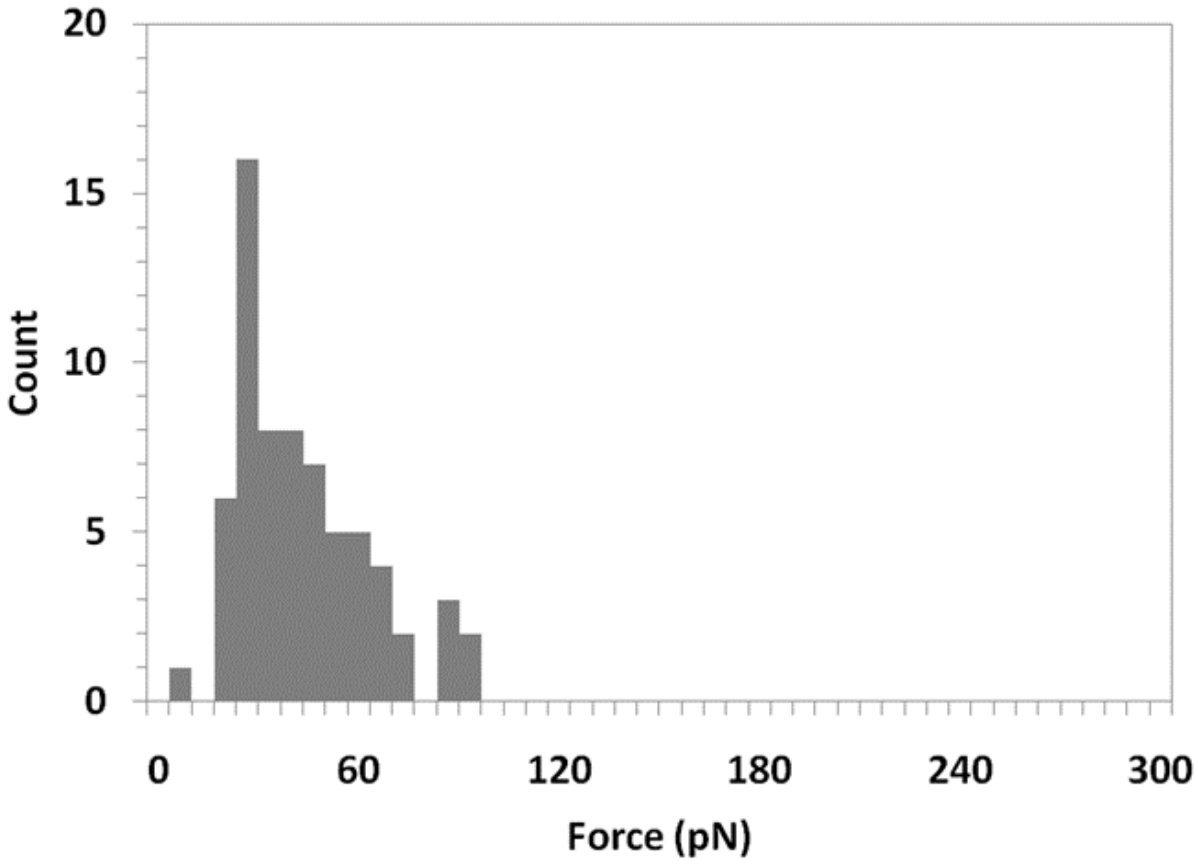

Figure 14 Rupture force distribution for the thrombin-poly(dA) complex at the lowest real loading rates (Avergae loading rate 90pN/s).

Autocorrelation of the force distributions were used to find the presence of a periodic pattern in the distributions [1, 47, 48] and to estimate the magnitude of the elementary binding force as a function of the loading rates [49]: The autocorrelation of the force distribution was computed according to:

$$R(\tau) = \int_{-\infty}^{\infty} p(F+\tau)\, p(F) dF \qquad \textbf{(1)}$$

Where R(τ) is the autocorrelation as a function of the force shift τ, $p(.)$ is the value of the force distribution.

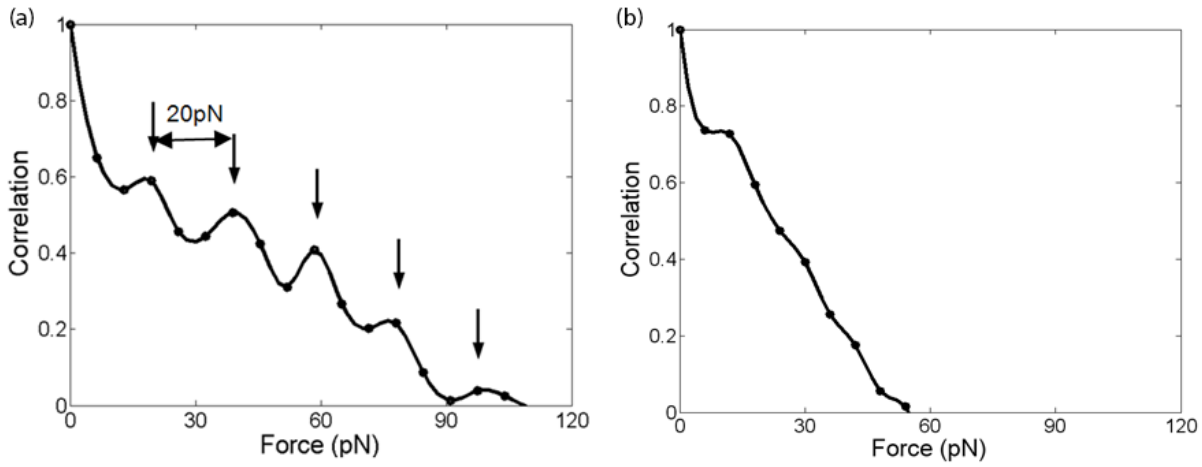

Figure 15: Computed autocorrelation of rupture force distribution at the lowest loading rate (Average loading rate 90pN/s) to highlight the observed periodicity in the histogram: (a) Autocorrelation for the histogram of rupture force distribution for Thrombin-aptamer complex; and (b) Autocorrelation for the histogram of rupture force distribution for Thrombin-poly(dA) complex.

For the sake of brevity, only the auto correlation functions for the force distribution corresponding to specific interaction at lowest loading rate (figure 13(a)) and non-specific interaction (figure 4) are plotted in figures 15(a) and (b), respectively. Periodically spaced peaks in auto correlation curve for the specific interaction (figure 15a) confirm the existence of the elementary binding force or the force quantum for specific binding. Similar periodically spaced peaks were observed in the autocorrelation function for other loading rate levels (See supplementary information). However, the auto correlation function did not show periodic patterns for nonspecific binding (figure 15b), indicating no characteristic force quantum involved in the force interaction between thrombin and poly(dA). The period of the repeating peaks in the autocorrelation curve shown in figure 15(a) was measured to estimate the force quantum for lowest real loading level. Similar analysis was utilized to estimate the

force quanta for other loading rates and the computed values are plotted as a function of the logarithm of the average loading rates in Figure 6.

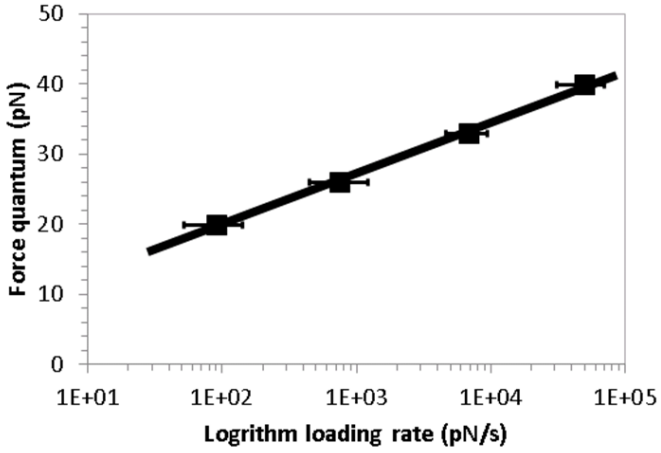

Figure 16 Plot of the force quantum determined from the experimentally measured rupture force histogram (SD: 29 pN/s for lowest loading rate; 165 pN/s for lower median loading rate; 1279 pN/s for higher median loading rate; 10322 pN/s for highest loading rate. n: 113 for each loading rate)

3.6 Results of Computational Simulation

Force displacement response were also computed form the simulation results of thrombin and aptamer unbinding under different displacement rates and a typical force displacement curve is provided in Appendix B..

It is complicated to determine the actual pulling velocities due to the bias in the dynamics, especially for a bimolecular system. To estimate the accelerated time, we fit our SMD data together with experimental data to a model introduced by Heymann and Grubmüller[50, 51], which approximates the dependence of the unfolding force F_{unbind} on the pulling velocity v of the cantilever by

$$F_{unbind} = \gamma v + \frac{k_B T}{L} l n(v/k_0 \Delta L)$$

(2)

Here, the friction of the water environment with friction coefficient γ dominates for fast pulling velocities (v > 1 m/s), whereas a logarithmic dependence of the unfolding force on the velocity applies for slow pulling velocities driven by the thermal energy k_BT. ΔL is the scatter width of the unfolding lengths L, and k_0 denotes the temperature-dependent rate of spontaneous dissociation in the absence of external forces.

Figure 17 shows the fitted curve to the equation 2 with the simulation vis a vis the experimental data with a 95% confidence interval and R^2 = 0.95. The parameters used in the fit are L = 2.5 Å and γ = 26.1 pN s/m; these values are in the range of typical SMD simulations.

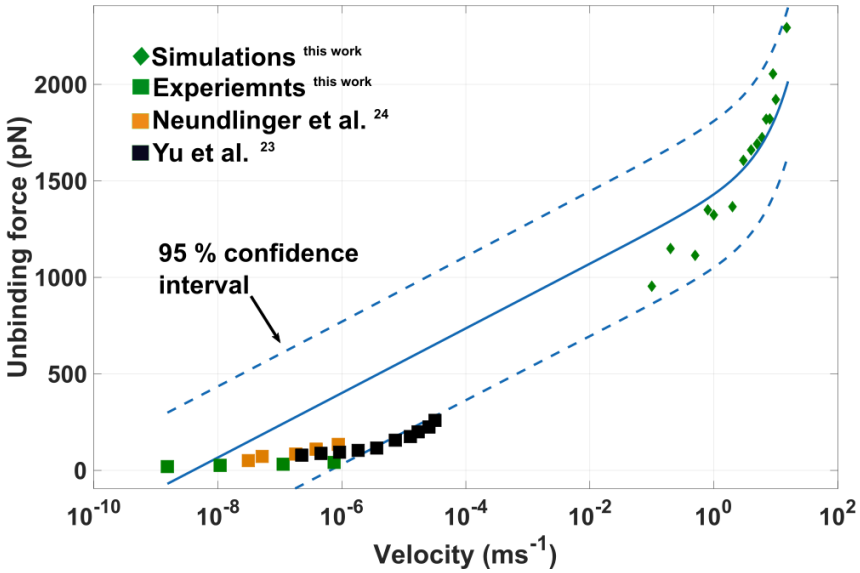

Figure 17 Plot of the fitted curve for the simulated as well as experimentally observed unbinding forces

For ΔL, the fit requires the relatively large value of ΔL = 1.12 × 10^{-5} computed force displacement curve showed similar characteristics as the experimental curves with monotonic

increase in loads with increased separation till the peak load. Computed peak loads are also plotted as a function of loading rates in Figure 6 in order to facilitate comparison between experimentally measured and computational predicted response. Although the pulling rates in the simulations are much faster (~ 1010 times) than those in experiments, they nevertheless follow a similar dependence on the loading rates indicating that simulations as well as experiments are able to capture the molecular mechanisms underlying the thrombin/aptamer unbinding.

The dissociation response of protein-aptamer binding with external load may be modeled using a single energy barrier model as proposed by Evans and co-workers [52-57]. When the thrombin-aptamer complex is not subjected to external loads, this energy barrier is quite high and results in a low probability for the complex to dissociate. When the bound complex is pulled apart under an external force, the work done by the force decreases the height of the energy barrier, and consequently increases the probability of dissociation. The probability of dissociation, p, may be expressed as a function of applied force, F as [52-57]:

$$p(F) = \frac{F_b}{r_f t_{off}} \exp\left\{ \frac{F}{F_b} - \frac{F_b}{r_f t_{off}} \left[\exp\left(\frac{F}{F_b} \right) - 1 \right] \right\}; \text{where } F_b = \frac{k_B T}{x_b} \quad \textbf{(3)}$$

r_f is the loading rate; t_{off} is the spontaneous dissociation time; F_β is the thermal force that dominates the spread of the distribution; and x_β is the width of the transition state barrier. According to equation (2), a peak in the probability distribution occurs when the exponential increase in failure rate due to applied force crosses over to the precipitous decline in bond survival with increasing force [55]. The rupture force, F_{peak}, corresponding to the peak of the probability distribution with respect to loading rate is determined to be:

$$F_{peak} = F_{\beta} \ln\left(\frac{r_f t_{off}}{F_{\beta}}\right) \quad \textbf{(4)}$$

The characteristic forces computed in auto-correlation analysis of the force histograms corresponds to F_{peak}'s at the different loading rates. The line obtained by fitting equation (4) to the measured peak forces is also plotted in Figure 6. The good agreement between the curve fit and both experimentally measured and computationally predicted data shows that equation (4) describes the observed response and that single energy barrier model described in equations (3) may be used to describe the protein-aptamer interaction. The slope and intercept of the fitted line were used to determine the values of the width of transition state barrier, x_{β}, to be approximately 0.8 nm and spontaneous dissociation time, $t_{\text{off,}}$ to be approximately 700 seconds. The estimated magnitude of the transition state barrier is comparable to the barrier width of 0.58 nm that characterizes 12 base DNA melting [27]. The magnitude for the dissociation time is also within the previously reported range of 500 to 10,000 seconds measured using electrochemical impedence assays for thrombin-aptamer dissociation [58]. These two results suggest that a single energy barrier model may be used to describe the thrombin-aptamer dissociation over the range of loading rates applied in these experiments and computational modelling.

The probability distribution in equation (4) corresponds to force expected from unbinding of a single bond and cannot be directly compared to the experimental data plotted in Figure 3 as the last unbinding force may be due to simultaneous rupture of more than one bond. In order to describe the experimentally measured force data, we make the following assumptions: rupture of individual bonds are independent; and the number of bonds in the last unbinding event follow a Poisson's distribution as the unbinding process occurred at a constant rate

over a given time interval [28]. Following the above assumptions, the probability distribution for multiple unbinding may be expressed as:

$$P(F) = \sum_{N=1}^{N_{\max}} p_{\lambda}(N) P_N(F) \quad \textbf{(5)}$$

Where *P(.)* is the probability density for rupture forces allowing unbinding of single as well as multiple bonds, F is the rupture force, p_{λ} is the weighting coefficient computed from Poisson distribution, N is the number of bond involved in the unbinding event, P_N is the probability density function for rupture force distribution with N number of dissociation bonds, which is the convolution of the single bond rupture force distribution expressed by equation (4). The parameter, λ, that describes the Poisson's distribution was estimated by fitting the equation (5) to experimental data corresponding to lowest loading rate as shown in figure 4(a) and was determined to be 2.5. The parameter value was used to predict the force distributions for other loading rates and the predicted probability distributions for other loading rates are compared to experimental data in Figure 13(b), (c) and (d). The predictions for multiple rupture force distribution based on equation (5) have a good agreement with the experimental histogram results. However, we should also point out that the Poisson distribution is a good estimate for the number of bonds when small number of bonds is involved in unbinding.

The characteristic rupture force of the thrombin-aptamer complex varies from 20 to 40 pN under mean loading rate variations from 90 to 45000 pN/s, which is larger than the earlier reported force value 4.45pN by Basnar et al [14] but smaller than 50 pN to 150 pN over a loading range of 500 pN/s to 20,000 pN/s reported by Neundlinger et al. [24]. Basnar et al.'s experiments [14] may have been influenced by steric hindrances in aptamer/protein complex

formation due to large surface density of protein and immobilized aptamers [24]. In order to eliminate the influence of steric hindrances, Neundlinger et al [24] utilized thrombin aptamer sequences that include a hybridized DNA linker part that enhances the binding between protein and the aptamer molecules and may have consequently measured larger dissociation forces. The force magnitudes presented in Figure 16 are comparable to the reported dissociation force for the unmodified aptamer sequence in range of 60-100 pN over faster loading rates varying from 12000 pN/s to 2×10^5 pN/s by Yu et al. [23]. However, It is difficult to make direct comparison of dissociation forces and loading rates becaues Yu et al. [23] have reported their results only as a function of the apparent loading rate (product of cantilever stiffness and displacement rate).

The magnitude of the characteristic forces in our experiment is similar to the forces of 23 to 40 pN corresponding to melting of a 12 base DNA duplex observed at loading rate ranging from 100 to 3000 pN/s [27, 59]. Lynch et al. [26] found the most likely unbinding force for disruption of G-quadruplex structure formed between two DNA strands to vary from 40 to 70 pN over similar loading rates as the current experiments. Yu et al. [60] found that a characteristic force of 23 – 29 pN is required to melt a G-quadruplex at loading with rates of 5 pN/s that are significantly lower than loading rates used in the current experiments. It should also be noticed that the thrombin aptamer used in this study forms a two G-tetrad quadruplex both in solution and in binding with thrombin. For the loading rates investigated in the current study, the magnitudes of characteristic forces associated with unbinding of the thrombin-aptamer complex are closer in magnitude to forces required for DNA melting than to those reported previously for disrupting G-quadruplex structures. In addition, the computational simulations that model the unbinding of aptamer and thrombin molecules

predict a similar dependence of rupture loads on loading rate as measured in the experiments. Hence, unbinding of the thrombin-aptamer complex may result from the breaking of bonds between aptamer and thrombin rather than disruption of the G-quadruplex structure of the aptamer.

3.7 Conclusions

AFM experiments were conducted to determine the characteristic force associated with specific binding between thrombin and its DNA aptamer. The measured rupture force distributions extend over a large magnitude of forces and demonstrate characteristics of force quanta for specific binding (thrombin-aptamer) in comparison to non-specific binding (thrombin-DNA). We find that the characteristic force for disruption of thrombin-aptamer complexes increases from 20 to 40 pN as the loading rate level increase from 100 to 40000 pN/s. Steered molecular dynamics simulation of the thrombin and apatamer unbinding also predicts similar dependence of the dissociation force on the loading rate as measured in experiments. The magnitude of characteristic forces is smaller than the previously reported force magnitudes associated with metling of the G-quadruplex structure. This difference suggests that, with the application of external force on the thrombin-aptamer complex, the G-quadruplex structure of the aptamer is not disrupted and the measured characteristic forces may be associated with dissociation of bonds between thrombin and the aptamer. The characteristic rupture forces were fitted to a single energy barrier model to extract the bond energy parameters associated with thrombin-aptamer binding, which is comparable to previously reported values obtained from different assays.

References

1. Florin, E.L., Moy, V.T. & Gaub, H.E. Adhesion Forces between Individual Ligand-Receptor Pairs. *Science* **264**, 415-417 (1994).
2. Oncins, G., Vericat, C. & Sanz, F. Mechanical properties of alkanethiol monolayers studied by force spectroscopy. *J Chem Phys* **128** (2008).
3. Strunz, T., Oroszlan, K., Schafer, R. & Guntherodt, H.J. Dynamic force spectroscopy of single DNA molecules. *P Natl Acad Sci USA* **96**, 11277-11282 (1999).
4. Flyvbjerg, H. Physics of bio-molecules and cells = Physique des biomolécules et des cellules: Les Houches session LXXV. (EDP Sciences; Springer, Les Ulis, 2002).
5. Tuerk, C. & Gold, L. Systematic Evolution of Ligands by Exponential Enrichment - Rna Ligands to Bacteriophage-T4 DNA-Polymerase. *Science* **249**, 505-510 (1990).
6. Ellington, A.D. & Szostak, J.W. Invitro Selection of Rna Molecules That Bind Specific Ligands. *Nature* **346**, 818-822 (1990).
7. Hermann, T. & Patel, D.J. Biochemistry - Adaptive recognition by nucleic acid aptamers. *Science* **287**, 820-825 (2000).
8. Gronewold, T.M.A., Glass, S., Quandt, E. & Famulok, M. Monitoring complex formation in the blood-coagulation cascade using aptamer-coated SAW sensors. *Biosens Bioelectron* **20**, 2044-2052 (2005).
9. Hianik, T., Ostatna, V., Zajacova, Z., Stoikova, E. & Evtugyn, G. Detection of aptamer-protein interactions using QCM and electrochemical indicator methods. *Bioorg Med Chem Lett* **15**, 291-295 (2005).
10. Lavrik, N.V., Sepaniak, M.J. & Datskos, P.G. Cantilever transducers as a platform for chemical and biological sensors. *Rev Sci Instrum* **75**, 2229-2253 (2004).
11. Stojanovic, M.N., de Prada, P. & Landry, D.W. Aptamer-based folding fluorescent sensor for cocaine. *J Am Chem Soc* **123**, 4928-4931 (2001).
12. Wallace, S.T. & Schroeder, R. In vitro selection and characterization of streptomycin-binding RNAs: Recognition discrimination between antibiotics. *Rna* **4**, 112-123 (1998).
13. Berens, C., Thain, A. & Schroeder, R. A tetracycline-binding RNA aptamer. *Bioorgan Med Chem* **9**, 2549-2556 (2001).
14. Basnar, B., Elnathan, R. & Willner, I. Following aptamer-thrombin binding by force measurements. *Anal Chem* **78**, 3638-3642 (2006).
15. Bock, L.C., Griffin, L.C., Latham, J.A., Vermaas, E.H. & Toole, J.J. Selection of Single-Stranded-DNA Molecules That Bind and Inhibit Human Thrombin. *Nature* **355**, 564-566 (1992).
16. Ge, L., Jin, G. & Fang, X.H. Investigation of the Interaction between a Bivalent Aptamer and Thrombin by AFM. *Langmuir* **28**, 707-713 (2012).
17. Griffin, L.C., Tidmarsh, G.F., Bock, L.C., Toole, J.J. & Leung, L.L.K. Invivo Anticoagulant Properties of a Novel Nucleotide-Based Thrombin Inhibitor and Demonstration of Regional Anticoagulation in Extracorporeal Circuits. *Blood* **81**, 3271-3276 (1993).
18. Tasset, D.M., Kubik, M.F. & Steiner, W. Oligonucleotide inhibitors of human thrombin that bind distinct epitopes. *J Mol Biol* **272**, 688-698 (1997).

19. Bode, W. et al. The Refined 1.9 a Crystal-Structure of Human Alpha-Thrombin - Interaction with D-Phe-Pro-Arg Chloromethylketone and Significance of the Tyr-Pro-Pro-Trp Insertion Segment. *Embo J* **8**, 3467-3475 (1989).
20. Tsiang, M., Gibbs, C.S., Griffin, L.C., Dunn, K.E. & Leung, L.L.K. Selection of a Suppressor Mutation That Restores Affinity of an Oligonucleotide Inhibitor for Thrombin Using in-Vitro Genetics. *J Biol Chem* **270**, 19370-19376 (1995).
21. Kelly, J., Feigon, J. & Yeates, T. Reconciliation of the X-ray and NMR structures of the thrombin-binding aptamer d(GGTTGGTGTGGTTGG). *J Mol Biol* **256**, 417-422 (1996).
22. Wu, Q., Tsiang, M. & Sadler, J.E. Localization of the single-stranded DNA binding site in the thrombin anion-binding exosite. *J Biol Chem* **267**, 24408-24412 (1992).
23. Yu, J., Jiang, Y., Ma, X., Lin, Y. & Fang, X. Energy Landscape of Aptamer/Protein Complexes Studied by Single-Molecule Force Spectroscopy. *Chemistry–An Asian Journal* **2**, 284-289 (2007).
24. Neundlinger, I. et al. Characterization of Enhanced Monovalent and Bivalent Thrombin DNA Aptamer Binding Using Single Molecule Force Spectroscopy. *Biophysical Journal* **101**, 1781-1787 (2011).
25. Miyachi, Y., Shimizu, N., Ogino, C. & Kondo, A. Selection of DNA aptamers using atomic force microscopy. *Nucleic Acids Res* **38** (2010).
26. Lynch, S., Baker, H., Byker, S.G., Zhou, D.J. & Sinniah, K. Single Molecule Force Spectroscopy on G-Quadruplex DNA. *Chem-Eur J* **15**, 8113-8116 (2009).
27. Pope, L.H. et al. Force-induced melting of a short DNA double helix. *Eur Biophys J Biophy* **30**, 53-62 (2001).
28. Erdmann, T., Pierrat, S., Nassoy, P. & Schwarz, U.S. Dynamic force spectroscopy on multiple bonds: Experiments and model. *Epl-Europhys Lett* **81** (2008).
29. Sader, J.E., Chon, J.W.M. & Mulvaney, P. Calibration of rectangular atomic force microscope cantilevers. *Rev Sci Instrum* **70**, 3967-3969 (1999).
30. Padmanabhan, K. & Tulinsky, A. An Ambiguous Structure of a DNA 15-mer Thrombin Complex. *Acta Crystallographica Section D* **52**, 272-282 (1996).
31. Hornak, V. et al. Comparison of multiple Amber force fields and development of improved protein backbone parameters. *Proteins: Structure, Function, and Bioinformatics* **65**, 712-725 (2006).
32. Perez, A. et al. Refinement of the AMBER force field for nucleic acids: improving the description of alpha/gamma conformers. *Biophysical journal* **92**, 3817-3829 (2007).
33. Jorgensen, W.L., Chandrasekhar, J., Madura, J.D., Impey, R.W. & Klein, M.L. Comparison of simple potential functions for simulating liquid water. *The Journal of Chemical Physics* **79**, 926 (1983).
34. Reshetnikov, R.V., Andrew, G., Vera, S., Alexei, K. & Jiri, S. Structural Dynamics of Thrombin-Binding DNA Aptamer d(GGTTGGTGTGGTTGG) Quadruplex DNA Studied by Large-Scale Explicit Solvent Simulations. *Journal of Chemical Theory and Computation* **6**, 3003-3014 (2010).
35. Ahmed, H.U. et al. The determination of protonation states in proteins. *Acta Crystallographica Section D* **63**, 906-922 (2007).

36. Berendsen, H.J.C., Spoel, D.v.d. & Drunen, R.v. GROMACS: A message-passing parallel molecular dynamics implementation. *Computer Physics Communication* **91**, 43-56 (1995).
37. Bussi, G., Donadio, D. & Parrinello, M. Canonical sampling through velocity rescaling. *J Chem Phys* **126**, 014101 (2007).
38. Berendsen, H.J.C., Postma, J.P.M., van Gunsteren, W.F., DiNola, A. & Haak, J.R. Molecular dynamics with coupling to an external bath. *The Journal of Chemical Physics* **81**, 3684 (1984).
39. Nosé, S. A unified formulation of the constant temperature molecular dynamics methods. *The Journal of Chemical Physics* **81**, 511 (1984).
40. Hoover, W. Canonical dynamics: Equilibrium phase-space distributions. *Physical Review A* **31**, 1695-1697 (1985).
41. Parrinello, M. & Rahman, A. Polymorphic transitions in single crystals: A new molecular dynamics method. *Journal of Applied Physics* **52**, 7182 (1981).
42. Isralewitz, B., Gao, M. & Schulten, K. Steered molecular dynamics and mechanical functions of proteins. *Current Opinion in Structural Biology* **11**, 224-230 (2001).
43. Lemkul, J.A. & Bevan, D.R. Assessing the stability of protofibrils using molecular dynamics. *Journal of Physical Chemistry B* **114**, 1652-1660 (2010).
44. Vemparala, S., Kalia, R.K., Nakano, A. & Vashishta, P. Electric field induced switching of poly(ethylene glycol) terminated self-assembled monolayers: A parallel molecular dynamics simulation. *J Chem Phys* **121**, 5427-5433 (2004).
45. Prime, K.L. & Whitesides, G.M. Self-Assembled Organic Monolayers - Model Systems for Studying Adsorption of Proteins at Surfaces. *Science* **252**, 1164-1167 (1991).
46. Michel, R., Pasche, S., Textor, M. & Castner, D.G. Influence of PEG architecture on protein adsorption and conformation. *Langmuir* **21**, 12327-12332 (2005).
47. Tromas, C. et al. Adhesion forces between Lewis(x) determinant antigens as measured by atomic force microscopy. *Angew Chem Int Edit* **40**, 3052-3055 (2001).
48. Schonherr, H. et al. Individual supramolecular host-guest interactions studied by dynamic single molecule force spectroscopy. *J Am Chem Soc* **122**, 4963-4967 (2000).
49. Kado, S. & Kimura, K. Single complexation force of 18-crown-6 with ammonium ion evaluated by atomic force microscopy. *J Am Chem Soc* **125**, 4560-4564 (2003).
50. Heymann, B. & Grubmüller, H. AN02/DNP-hapten unbinding forces studied by molecular dynamics atomic force microscopy simulations. *Chem Phys Lett* **303**, 1-9 (1999).
51. Grubmuller, H., Heymann, B. & Tavan, P. Ligand Binding: Molecular Mechanics Calculation of the Streptavidin-Biotin Rupture Force. *Science (New York, N.Y.)* **271** (1996).
52. Evans, E. Energy landscapes of biomolecular adhesion and receptor anchoring at interfaces explored with dynamic force spectroscopy. *Faraday Discuss* **111**, 1-16 (1998).
53. Evans, E.B. Looking inside molecular bonds at biological interfaces with dynamic force spectroscopy. *Biophys Chem* **82**, 83-97 (1999).
54. Merkel, R., Nassoy, P., Leung, A., Ritchie, K. & Evans, E. Energy landscapes of receptor-ligand bonds explored with dynamic force spectroscopy. *Nature* **397**, 50-53 (1999).

55. Evans, E. Probing the relation between force - Lifetime - and chemistry in single molecular bonds. *Annu Rev Bioph Biom* **30**, 105-128 (2001).
56. Evans, E., Leung, A., Hammer, D. & Simon, S. Chemically distinct transition states govern rapid dissociation of single L-selectin bonds under force. *P Natl Acad Sci USA* **98**, 3784-3789 (2001).
57. Moy, V.T., Florin, E.L. & Gaub, H.E. Intermolecular Forces and Energies between Ligands and Receptors. *Science* **266**, 257-259 (1994).
58. Li, X.X. et al. Electrochemical impedance spectroscopy for study of aptamer-thrombin interfacial interactions. *Biosens Bioelectron* **23**, 1624-1630 (2008).
59. Koch, S.J. & Wang, M.D. Dynamic force spectroscopy of protein-DNA interactions by unzipping DNA. *Phys Rev Lett* **91** (2003).
60. Ryu, J.-J. & Shrotriya, P. Roughness Evolution of Metallic Implant Surfaces Under Contact Loading and Nanoscale Chemical Etching: Influence of Surface Roughness and Contact Loading. (2009).

CHAPTER 4. GENERAL CONCLUSION

The present work utilizes a multiscale computation framework to analyze the interaction between thrombin and TBA-15 coated surface under the application of electrostatic potential. A continuum model for the monomolecular film aptamers immobilized on the electrode surface has been prepared based on the Poisson-Boltzmann equation and the polymer brush theory. The nature and magnitude of the electric field inside the aptamer layer is determined for different electrode potentials. The electrostatic force acting on a single aptamer strand is calculated for different electrode voltages for understanding the variation of the force with respect to aptamer length and grafting density. The computed electric fields are utilized in all atom molecular dynamics (MD) simulations (using GROMACS 4.6.7) involving the thrombin-aptamer complex for calculating the free energy of binding between the thrombin and TBA-15 in presence of different electric fields vis-à-vis the simple case of no electric field.

From the continuum modelling we could understand the nature of the electric field generated in the aptamer and the calculated force on a single aptamer corroborated the experimental observations. The MD study found that the free energy of binding decreases for applied positive electric fields, whereas it increases in presence of negative electric fields which lends support to the experimental observations.

Also, an analytical model connecting the simulation as well as AFM experiments for the forced unbinding of TBA/thrombin complex is utilized to understand the contribution of various parameters on the dissociation of the complex. It is found that the analytical model is able to predict the force response for very slow pulling rates within a 95% confidence

interval. It is to be noted that the entire DFS is presented to fall into two regimes, (i) activated and (ii) friction. Activated processes appear to dominate for pulling velocities smaller than 1 m/s. For very large pulling velocities in the range of 20 m/s, the friction forces contribute mostly with a vanishing role played by the activated regime. The analytical model is able to capture and thus predict the dynamics of the complex in the millisecond timescale of AFM experiments whereas the simulations are carried out in nanosecond timescale.

Future work

(i) To mimic the covalently attached TBA, the entire atomic structure has been restrained in the electric field MD simulations and pulling i.e. SMD simulations. The effect of electric field or pulling on the G-quadruplex structure of the TBA and thrombin could be investigated by only restraining the rest of the molecular structure.

(ii) The analytical function utilized the fit the AFM experiments described in Chapter 3, is able to predict the experimental forces with an error of 5%. This could be reduced by utilizing advanced SMD techniques like accelerated MD and/or newer potentials.

APPENDIX A. EFFECT OF ELECTRICAL STIMULUS ON THROMBIN APTAMER COMPLEX

A1: Effect of DNA layer condensation on the electrical field near the gold surface.

We approximated the effect of the condensation or folding of DNA layer using two assumptions: (1) the 15-mer TBA retain their G-quadraplex structure since the aptamer structure is stabilized on binding with thrombin protein; and (2) The charge distribution of the 35-mer linker layer is distributed over shorter distance as the linker chains fold near the surface. The calculations are performed for the different densities of DNA layers namely, = 10^{11} and 10^{12} cm^{-2}. These results show that for all the surface densities, the trends of electrical field dependence on the surface potential remain the same but the magnitudes of electrical fields increase with chain folding or condensations. Thus the results with rod-like fully stretched chains provide us with lowest estimate for the field magnitude.

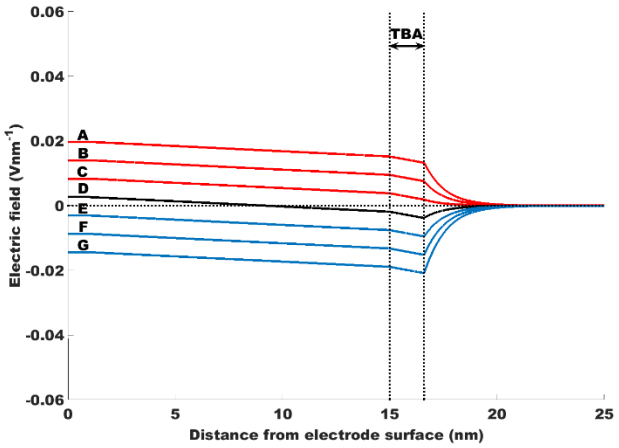

Figure 18 (a)

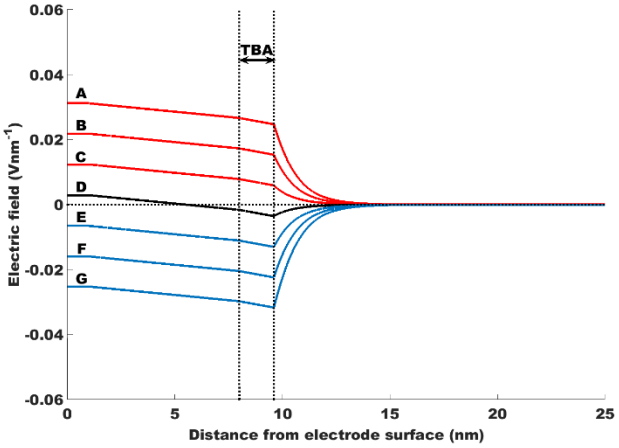

Figure 18 (b)

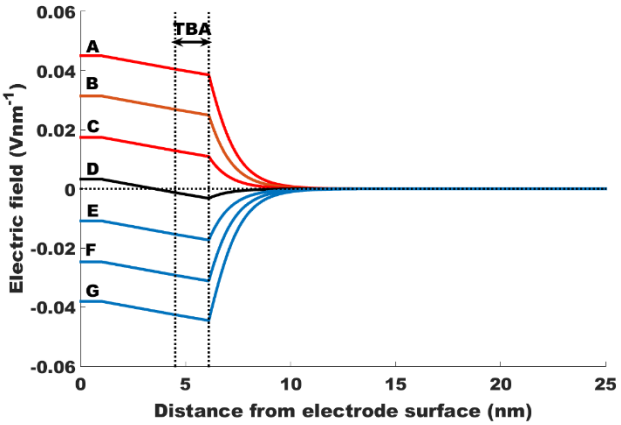

Figure 18 (c)

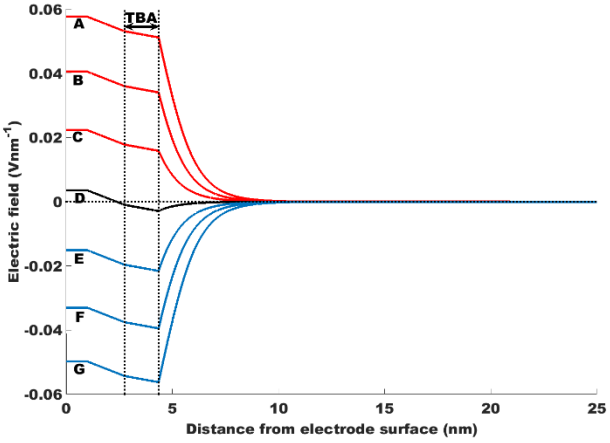

Figure 18 (d)

We consider the case where the nucleic acid grafting density is σ = 1011 cm-2. In chapter 2, Figure 5b corresponds to a fully stretched nucleic acid. As the structure of TBA (15-mer aptamer) is maintained upon thrombin binding as well as in salt solution12, we may look at cases where the 35-mer linker molecule (Figure 1(b)) is condensed upon itself, thus reducing the effective length of the structure. Figure 18 (a), 18 (b), 18 (c) and 18 (d) corresponds to the uncondensed/folded length and 1/2, 1/4th and 1/8th of the original linker length. It is observed that for increasing positive electrode potentials the electric field at the top of the nucleic acid layer becomes more positive thus corroborating our experimental observations. Curves A, B, C, D, E, F and G respectively correspond to the electrode potential of +300

mV, +200 mV, +100 mV, 0 mV, -100 mV ,-200 mV and -300 mV .The domain occupied by the 15-mer TBA is marked in the figure. Curves for the positive, neutral and negative electrode potentials are colored red, black and blue respectively.

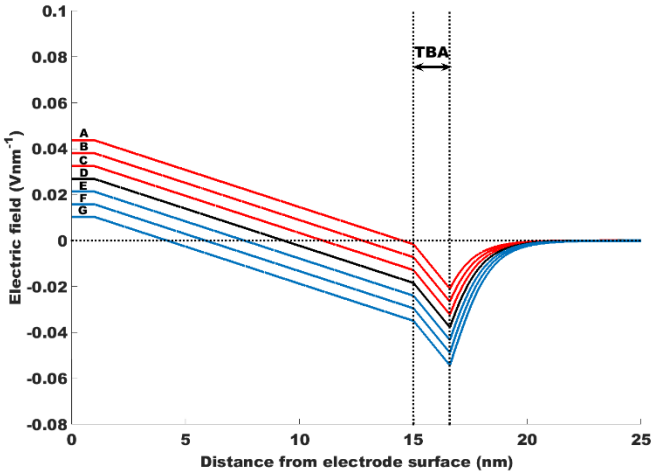

Figure 18 (e)

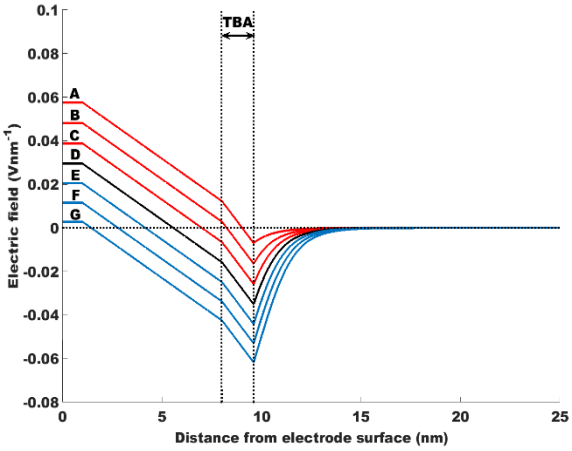

Figure 18 (f)

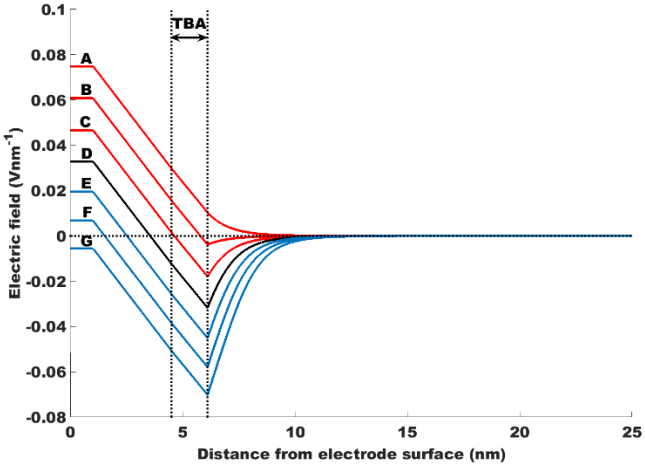

Figure 18 (g)

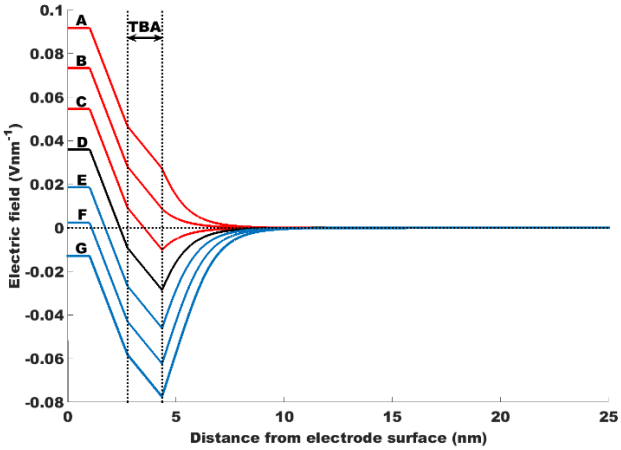

Figure 18 (h)

We consider the case where the nucleic acid grafting density is $\sigma = 10^{12}$ cm^{-2}. Similar observations are observed as in the case discussed for $\sigma = 10^{11}$ cm^{-2} . It is to be noted that on account of greater surface density of nucleic acid the positive nature of the electric field is more expressed for greater condensation of linker for the corresponding electrode potentials. Figure 18 (e), 18 (f), 18 (g) and 18 (h) corresponds to the uncondensed/folded length and 1/2, 1/4th and 1/8th of the original linker length. It is observed that for increasing positive electrode potentials the electric field at the top of the nucleic acid layer becomes more

positive thus corroborating our experimental observations. Curves A, B, C, D, E, F and G respectively correspond to the electrode potential of +300 mV, +200 mV, +100 mV, 0 mV, -100 mV, -200 mV and -300 mV. The domain occupied by the 15-mer TBA is marked in the figure. Curves for the positive, neutral and negative electrode potentials are colored red, black and blue respectively.

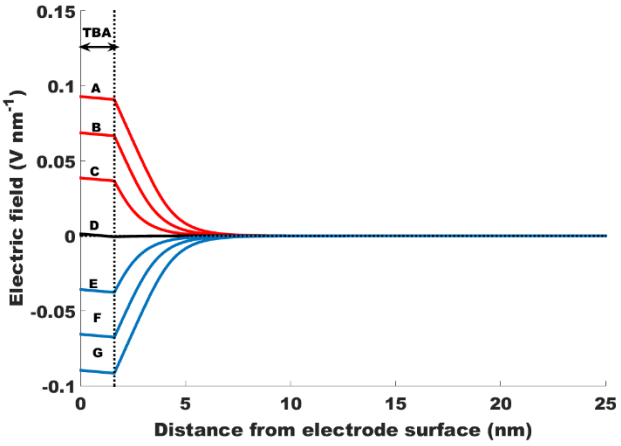

Figure 18 (i)

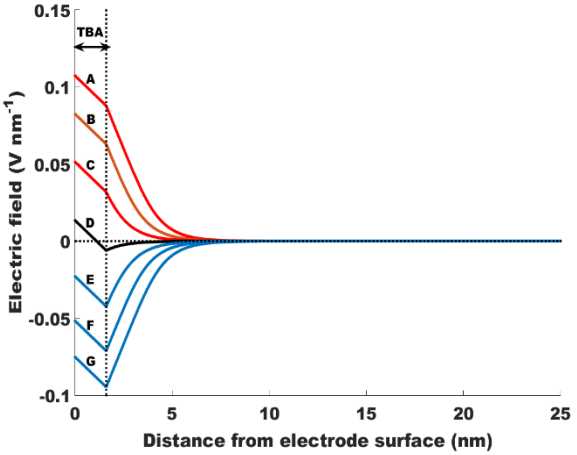

Figure 18 (j)

If we only consider, the 15-mer aptamer for the continuum modeling, we find that at (+) 100 mV for $\sigma = 10^{11}$ cm^{-2}, the field at the top of the layer is ~ 0.04 Vnm^{-1} (Figure 18 (i)) and that for $\sigma = 10^{12}$ cm^{-2} is ~ 0.03 Vnm^{-1}(Figure 18 (j)). This is thus an order of magnitude higher than the cases with the 35-mer linker molecule as discussed previously. In the MD simulations, only the 15-mer aptamer is included, and, the positive field at which dissociation is observed is about 10 times i.e. one order of magnitude higher than the electric field calculated from the continuum modeling. This difference is attributed to the large disparity in

the time scale of the experiments and the atomistic simulations, as discussed in the main article.

In Figures 18(i) and 18(j), curves A, B, C, D, E, F and G respectively correspond to the electrode potential of +300 mV, +200 mV, +100 mV, 0 mV, -100 mV, -200 mV and -300 mV. The domain occupied by the 15-mer TBA is marked in the figure. Curves for the positive, neutral and negative electrode potentials are colored red, black and blue respectively.

A4: Choice of pulling velocities in electric field SMD simulations

Evidence in the literature suggest that the application of slower/faster pull rates result in almost identical trajectories and qualitatively similar force-time curves [1]. In practice, a convenient pulling rate is used to expedite data collection while maintaining the reliability of the procedure and ensuring that no artifacts are introduced in the results. We find that at high ((+) 1.0 and (+) 0.5 V nm^{-1}) positive electric fields using a pulling rate of 0.01 nm ps^{-1} resulted in the COM separation distance between the TBA and the thrombin to be greater than half of the box dimension along the z axis. This violates the convention for the periodic boundary condition of a rectangular simulation box. Hence, a relatively slower pull rate is employed. Table 2 lists the details of the umbrella sampling simulations on the SMD trajectories for (±) 0.5 V nm^{-1} and (+) 1.0 V nm^{-1} cases.

Table 2: Comparison of different US simulations

Electric field (Vnm^{-1})	Umbrella sampling windows	Total simulation time (ns)	Pull rate (nm ps^{-1})	COM separation (nm)
0	**42**	**424.2**	**0.010**	**5.50**
(+) 0.5	**38**	**383.8**	**0.008**	**4.90**
(+) 1.0	**34**	**343.4**	**0.006**	**4.01**
(-) 0.5	**41**	**414.1**	**0.010**	**5.36**

A5: Choice of restraining potential for umbrella sampling:

Pagano et.al studied the thermodynamics of the interaction of TBA with thrombin through isothermal titration calorimetry (ITC) experiments[2]. They assumed a single set of equivalent binding sites to determine the binding constant from which the binding Gibbs energy change was calculated. At 25 ^{o}C , the $\Delta G_{binding}$ calculated by them was about 9 kcalmol^{-1}. The $\Delta G_{binding}$ calculated by Yang et al., from MD simulations, puts the value at 17 kcalmol^{-13}. The ITC experiments did not permit a distinction between the two binding sites of thrombin as the titration data do not have distinct energy profiles and the value was measured based on the relative populations of the complex and non-complex forms. The Yang group argues that the $\Delta G_{binding}$ predicted by the MD simulations is larger than the experimental one because the simulation value is the free energy cost for a full separation of TBA from thrombin [3]. They also used a very high force constant of 12560.4 kJmol^{-1}nm^{2} and in their study the pulling coordinate is taken as the bond distance of the COM of TBA and the other end is the COM of the protein residues (Glu77-Lys81) enclosed by the TT loops of TBA. In the present study we instead take a much lower force constant of 1000 kJmol^{-1}nm^{2} and our pulling coordinate is also different as described previously in the methodology section. We find that using a reduced force constant does not affect the convergence of the PMF. AFM pulling techniques have been utilized to unfold biomolecules like DNA hairpins to map the folding energy landscape by conducting equilibrium constant-force reversible folding-unfolding measurements. However AFM pulling experiments and data for TBA/thrombin complex, providing the $\Delta G_{binding}$, is still not available. From the theory of the umbrella sampling method it is understood that the ideal restraining potential would be the negative of the exact PMF, which is unknown for the present problem. When the negative of the exact PMF is

used as the biasing potential it flattens the energy landscape and thus avoids the problem of getting trapped by large energy barriers. In absence of experimental data, researchers have used adaptive umbrella sampling method, multicanonical sampling method and the entropy sampling method, which unfortunately entail a lot of computational cost[4, 5].

All points along the reaction coordinate are to be sufficiently sampled for the WHAM method to produce a converged PMF. A necessary check for the convergence is the overlap and smoothness of the histograms generated from sampling of the reaction coordinate[6, 7]. The stipulation of this check ensures that all points along the reaction coordinate are thoroughly sampled in multiple simulation windows. These considerations determine the positioning of the umbrella sampling windows and the strength of the biasing potential i.e. the force constant. Proper sampling and thus the smoothness of the generated histograms also depends on the simulation time which is again constrained by computational costs. We have used an umbrella sampling simulation time of 10 ns per window against the 20 ns mentioned in the work by the Yang group[3]. We find that this does not greatly influence the smoothness of the umbrella sampling histograms. The histograms generated for the US simulations in the present study are shown in Fig. 29. An optimum simulation framework that can minimize simulation cost and still preserve the accuracy of the generated results will greatly depend on the nature of the system on which the MD simulations are performed.

A6: Average over MD simulations

Each of the 5 ns electric field MD simulations and the 500 ps SMD simualtions were carried out 5 times to check the average behavior of the system under the different cases of electric field. The observations are represented in a tabular form as below:

Table 3: Comparison of H-bond count for different electric field MD simulations

Electric field (Vnm^{-1})	Average H-bond count per frame of a 5 ns electric field MD simulation					
	#1	#2	#3	#4	#5	Average
(+) 0.1	5.54	5.31	5.78	5.82	5.45	5.58
(+) 0.5	1.48	1.37	1.68	0.98	1.52	1.41
(+) 1.0	0.48	0.91	1.29	0.68	0.72	0.82
(-) 0.5	3.26	2.53	3.35	3.49	3.16	3.16
(-) 1.0	7.65	7.16	7.70	7.78	7.71	7.60

It is observed that with increasing positive electric field the H-bond count per simulation frame decreases whereas for the high negative field of (-) 1.0 Vnm^{-1} because of reorientation of protein and promotion of newer interactions the H-bond count increases. At (-) 0.5 Vnm^{-1}, the protein drifts away from the TBA and thus lesser H-bonds are formed towards the last part of the simulation.

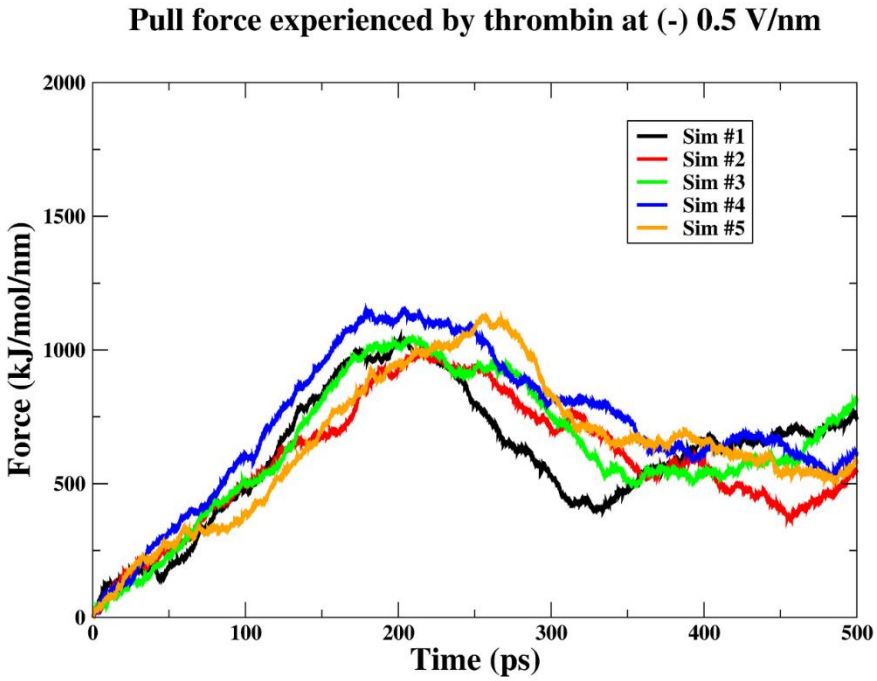

Figure 19

The above figure shows the pull force experienced by the COM of thrombin under the electric field of (-) 0.5 Vnm^{-1}. The 5 curves are from 5 different SMD simulations. The maximum force obtained from each of these 5 simulations are mentioned in Table 3.

Table 4: Comparison of peak forces obtained from different electric field SMD simulations

Electric field (Vnm^{-1})	Peak force obtained from a 500 ps SMD simulation (kJmol^{-1}nm^{-1})					
	#1	#2	#3	#4	#5	Average
0	1079.46	914.62	1120.32	1127.31	1053.71	1059.08
(+) 0.5	668.09	807.48	752.66	769.45	768.81	753.30
(+) 1.0	460.29	322.48	512.68	482.96	581.39	471.96
(-) 0.5	1041.32	996.95	1047.54	1154.89	1129.01	1073.94

We find that from the average values of the 5 simulations that the peak force experienced by the COM of the thrombin during the SMD simulations are progressively lesser in magnitude with increasing positive electric field. It is also noted that the peak force for the electric field of (-) 0.5 Vnm^{-1}, is somewhat higher than that observed in the neutral case.

Exclusion of ligand OG6 from initial topology of MD simulations

The ligand OG6 was excluded from the coordinate of the PDB file 1HAO while preparing the topology of the MD simulation. The small molecule OG6 is an inhibitor called D-Phe-Pro-Arg-chloromethylketone (PPACK)[8]. It has got nonstandard residues which do not conform to the force field parameters used in the present study. OG6 is not associated with exosite-I of thrombin and the TBA/thrombin complex is found to be stable (without OG6) for long MD simualtions as described in figure S3. More details about OG6 are provided in the paper by Maitz et al. [8].

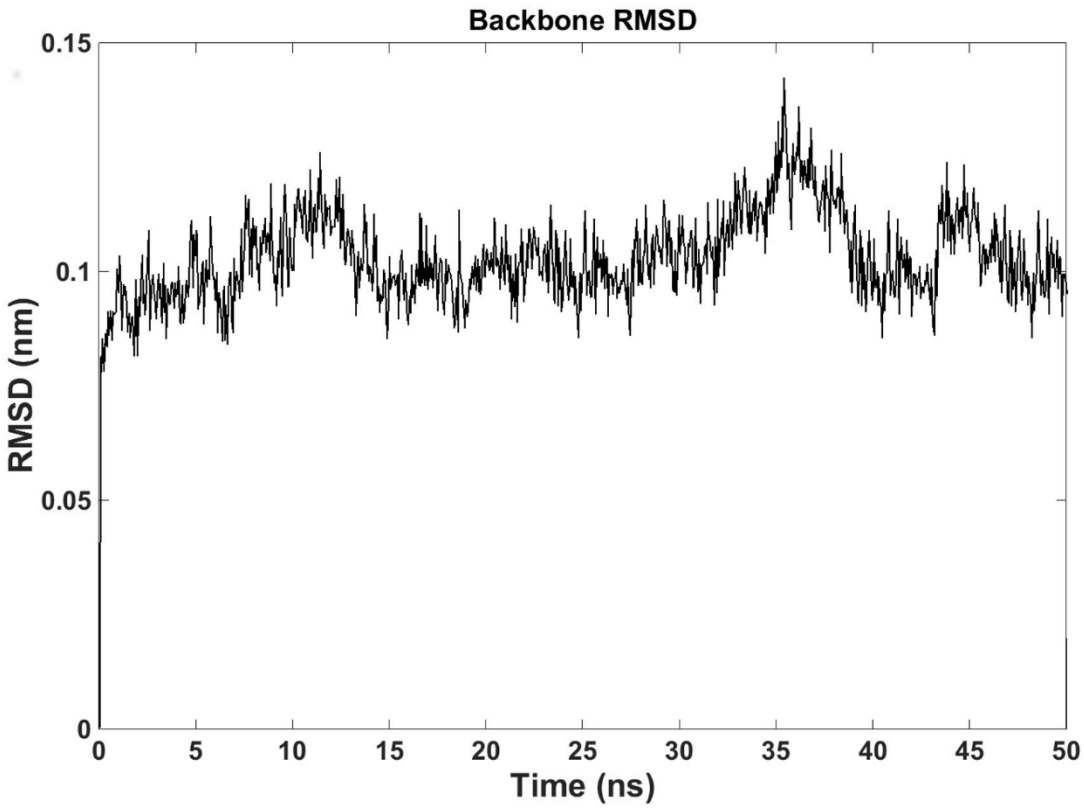

Figure 20

The time evolution of backbone RMSD of thrombin, calculated with respect to the crystal structure, over the 50 ns unrestrained MD simulation is represented. The low average RMSD value of ~ 0.13 nm shows that the thrombin is stable over long simulation time. The ligand OG6 (used as an inhibitor for thrombin in laboratory applications) is excluded at the beginning of solvation as it does not interfere with the exosite-I of thrombin and the parameterization of non-standard residues could be avoided. However, it is imperative to check the stability of thrombin-aptamer complex on removal of a certain ligand molecule and hence the 50 ns simulation provided conclusive evidence for the same.

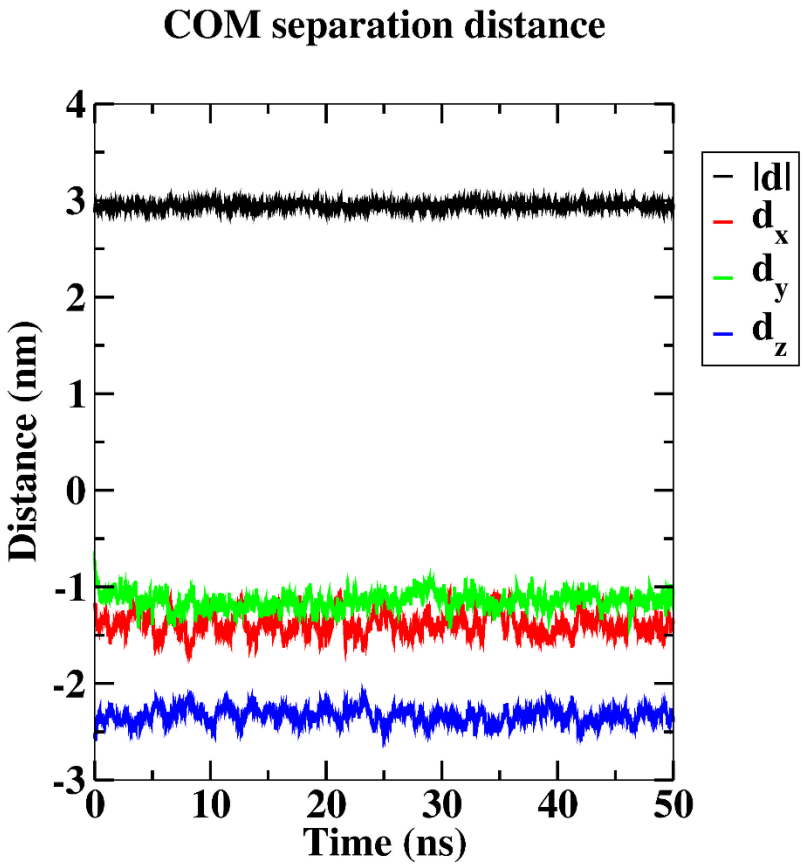

Figure 21

The time evolution of the COM separation between TBA and thrombin is shown for a 50 ns MD simulation where the system was put under an electric field of (+) 0.1 Vnm^{-1}. The TBA is position restrained while the thrombin is free to move. However, it is observed that the COM separation (including the *x*, *y* and *z* components) is constant indicating that the TBA/thrombin complex did not dissociate. Same could be observed from the visualization of the simulation.

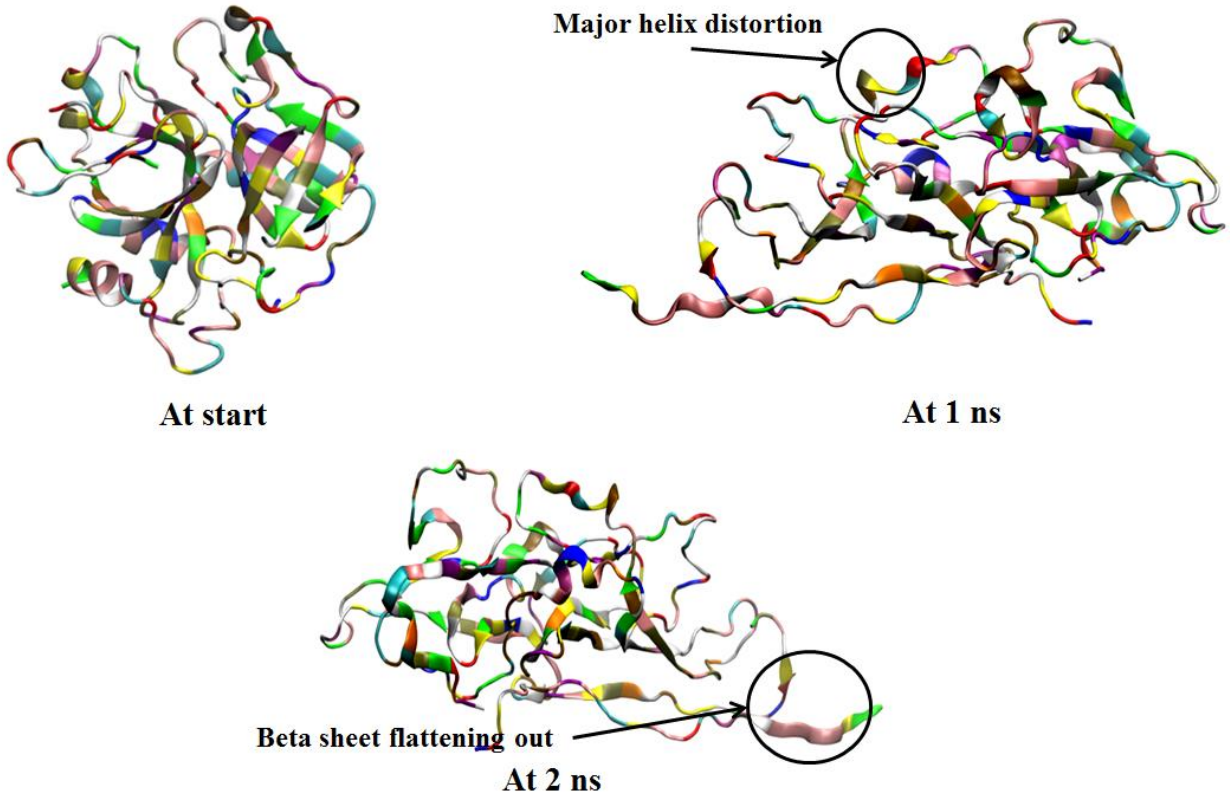

Figure 22

The effect of (+) 3.0 Vnm^{-1} electric field on the structure of thrombin, as observed from the visualization of the corresponding MD simulation is shown. All images are rendered in VMD[10] . The protein structure deteriorates rapidly with increase in simulation time in presence of the strong electric field.

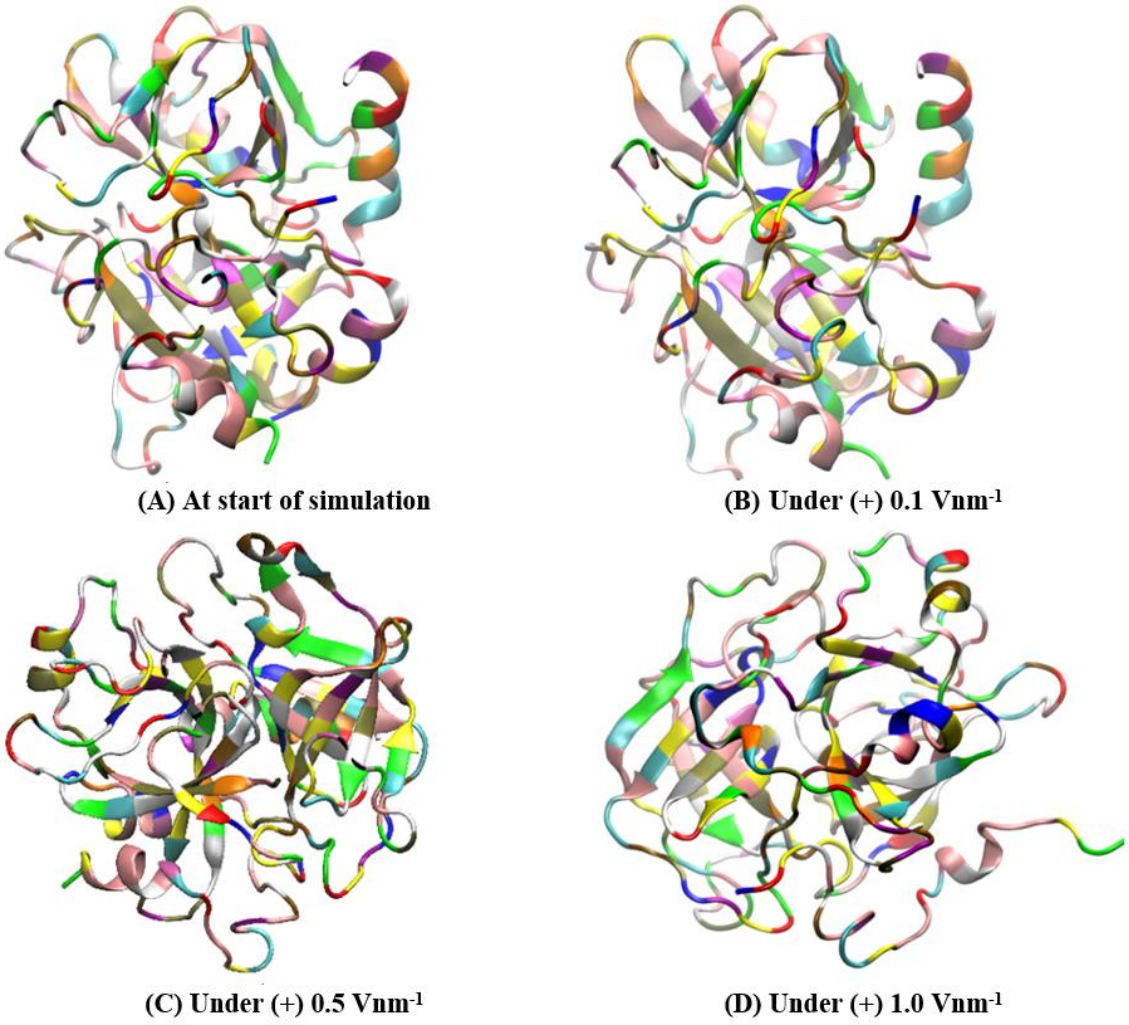

Figure 23

The comparative images obtained from the visualization of the positive electric field simulation on the thrombin-aptamer complex is shown. The snapshots are produced from the end of the 5 ns simulation. The designation is as follows: A: 0 Vnm^{-1}, B: (+) 0.1 Vnm^{-1}, C: (+) 0.5 Vnm^{-1}, D: (+) 1.0 Vnm^{-1}. It is observed that at higher fields there is gradual unfolding of thrombin due to distortion in protein secondary structure. The alpha helices and the beta sheets are found to be distorted to a greater extent with increasing electric field magnitude. The unfolding of the protein results in higher RMSD values as observed in Fig. 6.

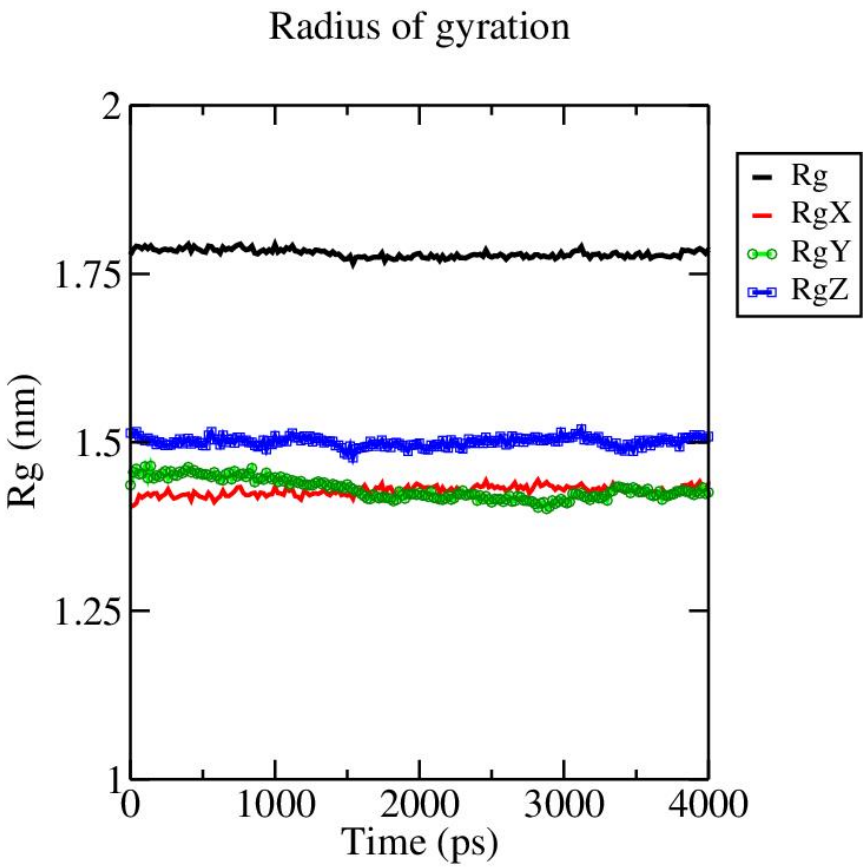

Figure 24

The time evolution of radius of gyration (R_g) of the thrombin protein under (+) 0.5 Vnm^{-1} electric field, calculated for 4 ns of the 5 ns simulation, is shown. The thrombin exited the simulation box and hence the last 1 ns is excluded. The radius of gyration may be described as the mass weighted scalar length of each atom from the center-of-mass (COM). From the above figure it can be seen that the $R_g$remains fairly constant throughout the simulation time and this confirms that the globular protein structure did not experience unfolding and retained its shape under the effect of the electric field.

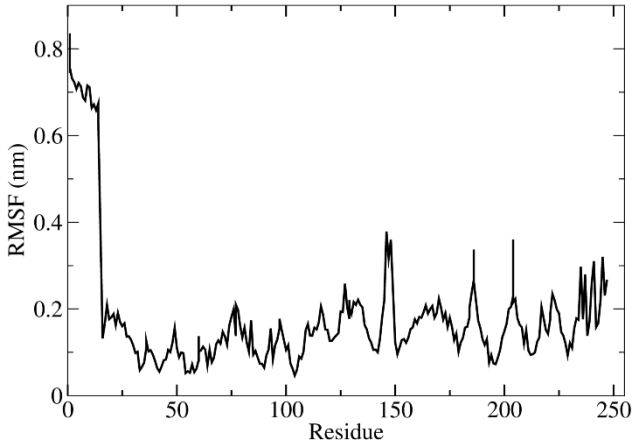

Figure 25

The time evolution of RMSF (Root Mean Square Fluctuation) of thrombin residues under (+) 0.5 Vnm^{-1} electric field calculated for the last 1 ns of MD simulation time (while thrombin was inside the simulation box) is shown. RMSF is the time-average of RMSD (Figure 6) for each residue and shows the dynamic behavior of each residue. The plot shows that the thrombin residues, particularly those at the start of the backbone chain are fluctuating more indicating the effect of the stress induced by the electric field.

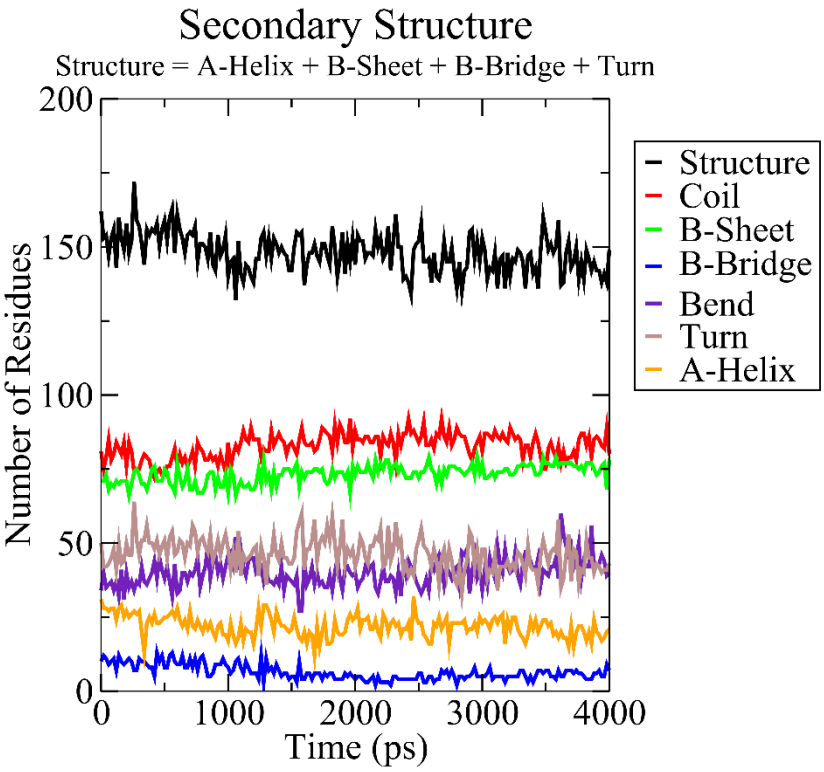

Figure 26

The secondary structure evolution of thrombin, in presence of (+) 0.5 Vnm^{-1}electric field is shown for the different residues till 4 ns of the 5 ns simulation. The thrombin exited the simulation box and hence the last 1 ns is excluded. It is noticed that even if the RMSD (Figure 6) and RMSF (Figure 25) show higher values due to the application of a moderately high positive electric field, the secondary structure does not change much. Secondary structure analysis is executed with the DSSP (Define Secondary Structure of Proteins) algorithm[11].

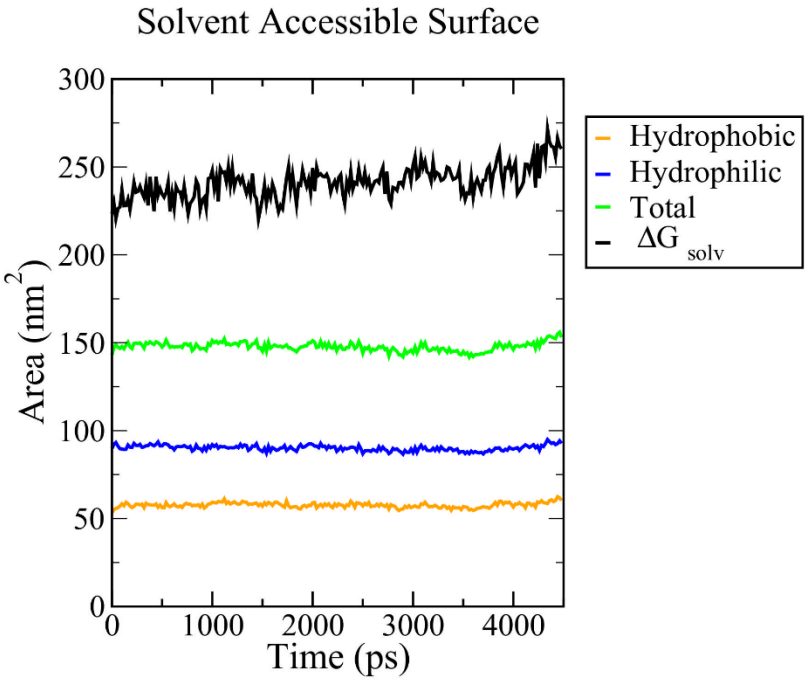

Figure 27

The SASA (Solvent Accessible Surface Area) calculation is shown for thrombin under (+) 0.5 Vnm^{-1} electric field. The thrombin exited the simulation box, upon unbinding from the TBA, and hence the last 1 ns is excluded. It is observed that the magnitude of the total protein surface area is almost conserved indicating that there is no ingress of solvent due to protein unfolding and the globular structure is maintained. As expected the $\Delta G_{solvation}$ for thrombin with respect to the water (solvent) is also conserved throughout the simulation.

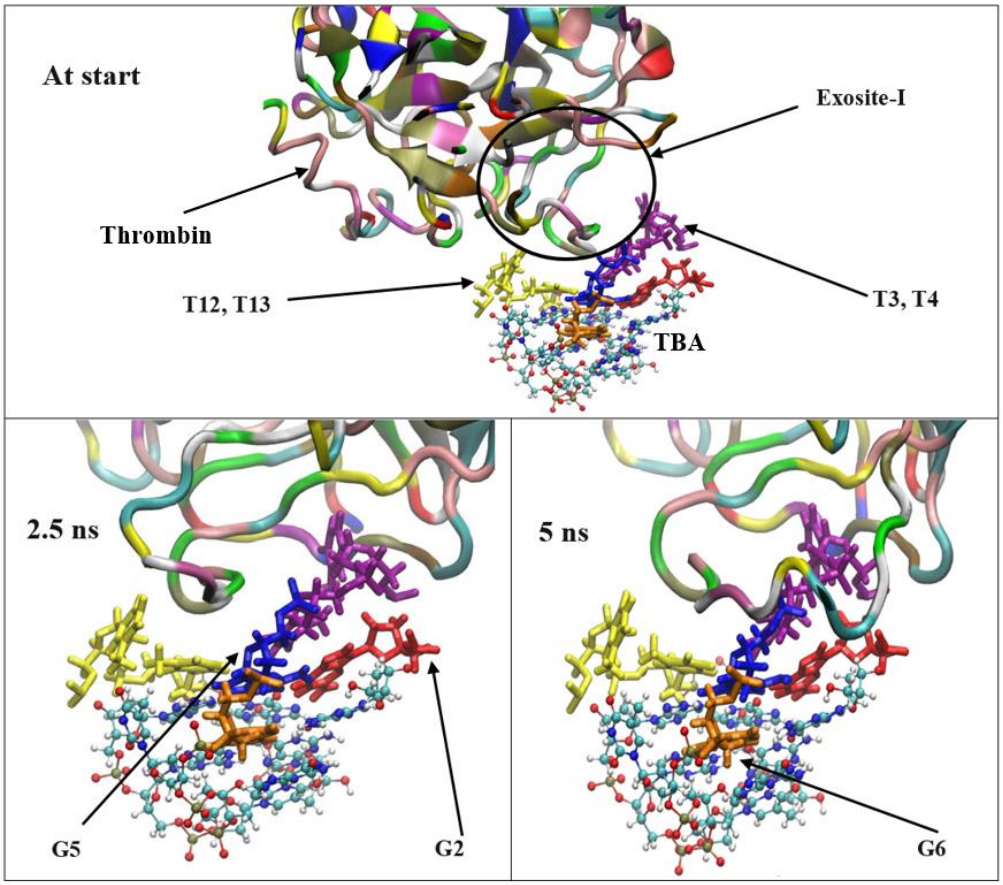

Figure 28

The association between the exosite-I residues of thrombin and the TT loops as well as the G2,G5 and G6 bases is observed in the MD simulation with an electric field of (-) 1.0 Vnm^{-1}. Normally the TBA interacts with the exosite-I residues through its TT loops. In the simulation the TBA was position restrained and the protein was allowed to move freely. As the simulation progressed the protein reoriented itself such that many new interactions were promoted because of the close proximity of the G2, G5 and G6 bases to the reoriented protein. All images are rendered in VMD[10]. The thrombin is represented in the New Cartoon format whereas the T12, T13 (yellow), T3, T4 (purple), G2 (red), G5 (blue) and G6 (orange) bases are represented in the licorice format. All other TBA bases are represented in the CPK format. For clarity of visualization, water molecules and ions are removed.

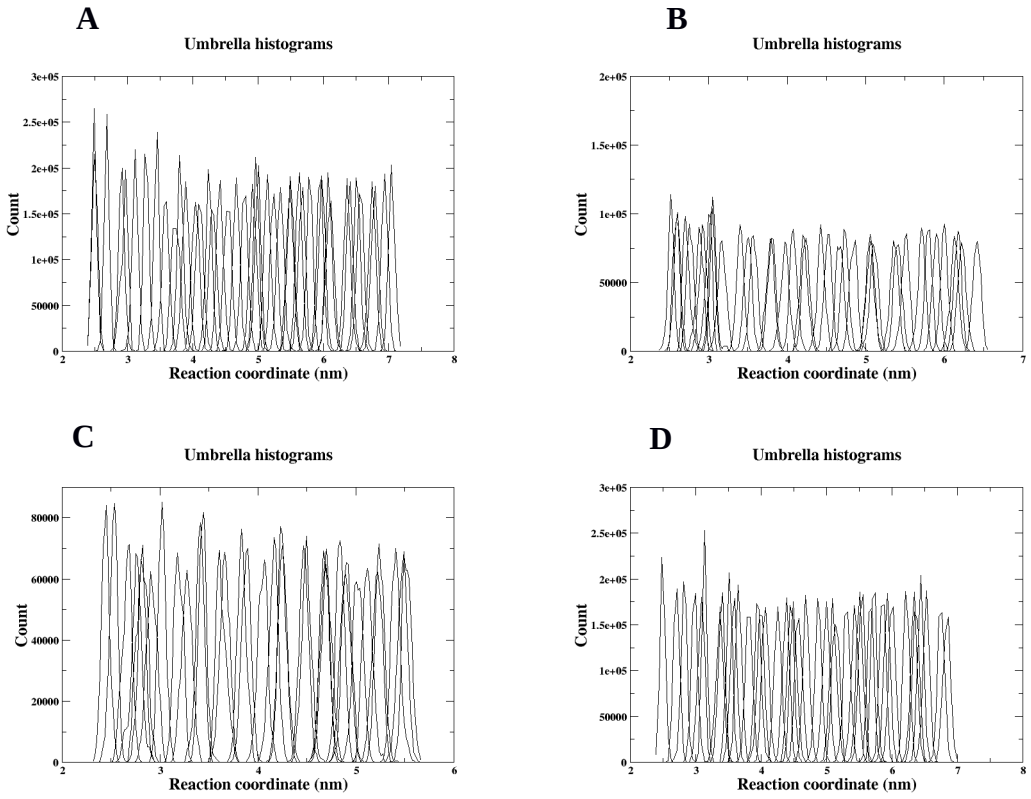

Figure 29 (a)

29 (a): Umbrella sampling histograms for the different SMD simulations discussed in Chapter 2 are given. The designation is as follows: A: 0 Vnm^{-1}, B: (+) 0.5 Vnm^{-1}, C: (+) 1.0 Vnm^{-1}, D: (-) 0.5 Vnm^{-1}.

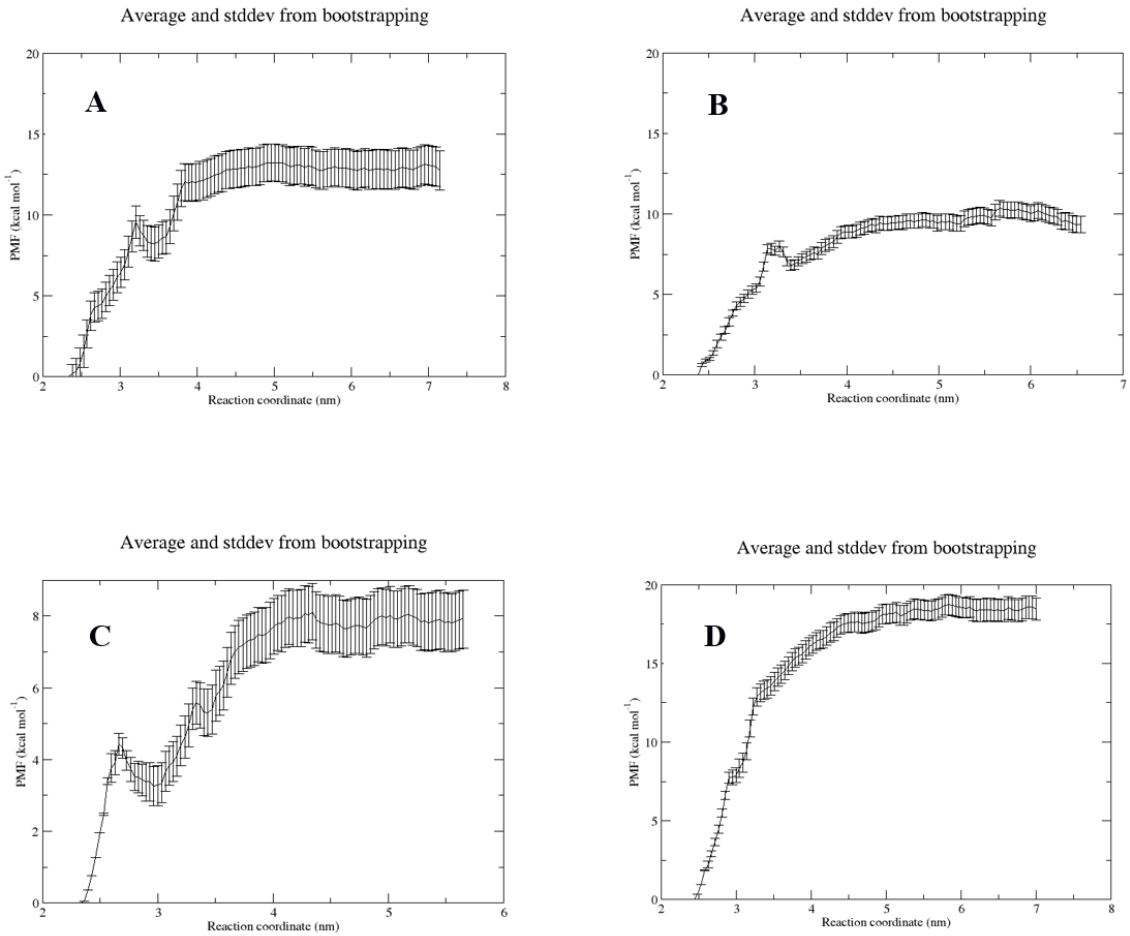

Figure 29 (b)

29 (b): Umbrella sampling bootstrap results with 100 bins for the different SMD simulations discussed in the text are given. The designation is as follows: A: 0 Vnm^{-1}, B: (+) 0.5 Vnm^{-1}, C: (+) 1.0 Vnm^{-1}, D: (-) 0.5 Vnm^{-1}. The length of the error bars is expected to decrease in length with longer sampling times.

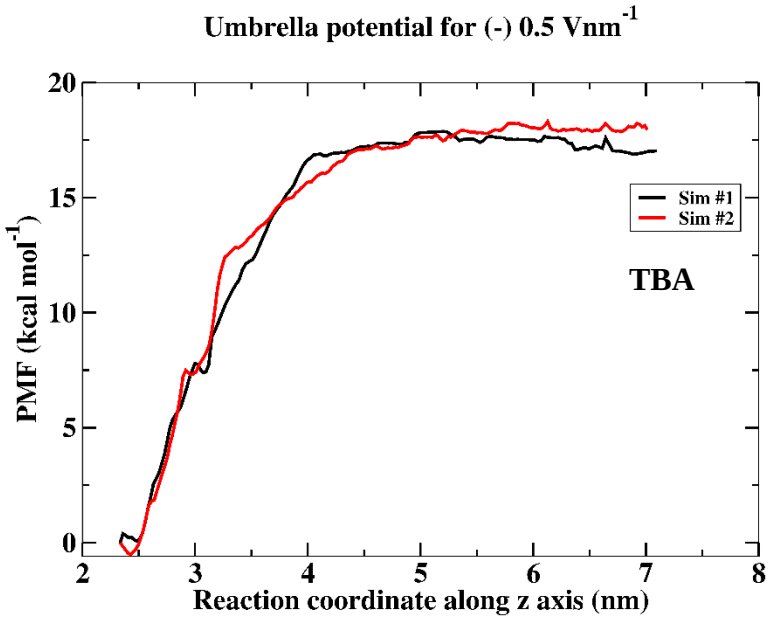

Figure 30

The PMF profile from two separate US simulations of the same SMD simulation trajectory is shown.

Our results for two different US simulations with the same parameters conducted on two different SMD simulation trajectories with identical starting system are repeatable and reproducible.

References

1. Lemkul, J.A. & Bevan, D.R. Assessing the stability of protofibrils using molecular dynamics. *Journal of Physical Chemistry B***114**, 1652-1660 (2010).
2. Pagano, B., Martino, L., Randazzo, A. & Giancola, C. Stability and binding properties of a modified thrombin binding aptamer. *Biophysical journal***94**, 562-569 (2008).
3. Kim, E., Yang, C. & Pak, Y. Free-Energy Landscape of a Thrombin-Binding DNA Aptamer in Aqueous Environment. *Journal of Chemical Theory and Computation***8**, 4845-4851 (2012).
4. Kästner, J. Umbrella sampling. *Wiley Interdisciplinary Reviews: Computational Molecular Science***1**, 932-942 (2011).
5. Mills, M. & Andricioaei, I. An experimentally guided umbrella sampling protocol for biomolecules. *J Chem Phys***129**, 114101 (2008).
6. Torrie, G.M. & Valleau, J.P. Nonphysical sampling distribution in Monte Carlo free energy estimation: umbrella sampling. *Journal of Computational Physics***23**, 187-199 (1977).
7. Hub, J.S., Groot, B.L.D. & Spoel, D.V.D. g_wham-A Free Weighted Histogram Analysis Implementation Including Robust Error and Autocorrelation Estimates. *Journal of Chemical Theory and Computation***6**, 3713-3720 (2010).
8. Maitz, M.F., Sperling, C. & Werner, C. Immobilization of the irreversible thrombin inhibitor D-Phe-Pro-Arg-chloromethylketone: A concept for hemocompatible surfaces? *Journal of Biomedical Materials Research Part A***94A**, 905-912 (2010).
9. Ma, X. in Mechanical Engineering, Vol. Doctor of Philosophy (Iowa State University, 2013).
10. Humphrey, W., Dalke, A. & Schulten, K. VMD: Visual molecular dynamics. *Journal of Molecular Graphics***14**, 33-38 (1996).
11. Kabsch, W. & Sander, C. Dictionary of protein secondary structure: Pattern recognition of hydrogen-bonded and geometrical features. *Biopolymers***22**, 2577-2637 (1983).
12. Radi, A.-E., Acero Sánchez, J.L., Baldrich, E. & O'Sullivan, C.K. Reagentless, Reusable, Ultrasensitive Electrochemical Molecular Beacon Aptasensor. *Journal of the American Chemical Society***128**, 117-124 (2006).
13. Stachowiak, J.C., Yue, M., Castelino, K., Chakraborty, A. & Majumdar, A. Chemomechanics of Surface Stresses Induced by DNA Hybridization. *Langmuir***22**, 263-268 (2006).

APPENDIX B. STEERED MOELCULAR DYNAMICS SIMULATIONS OF THROMBIN-APTAMER COMPLEX

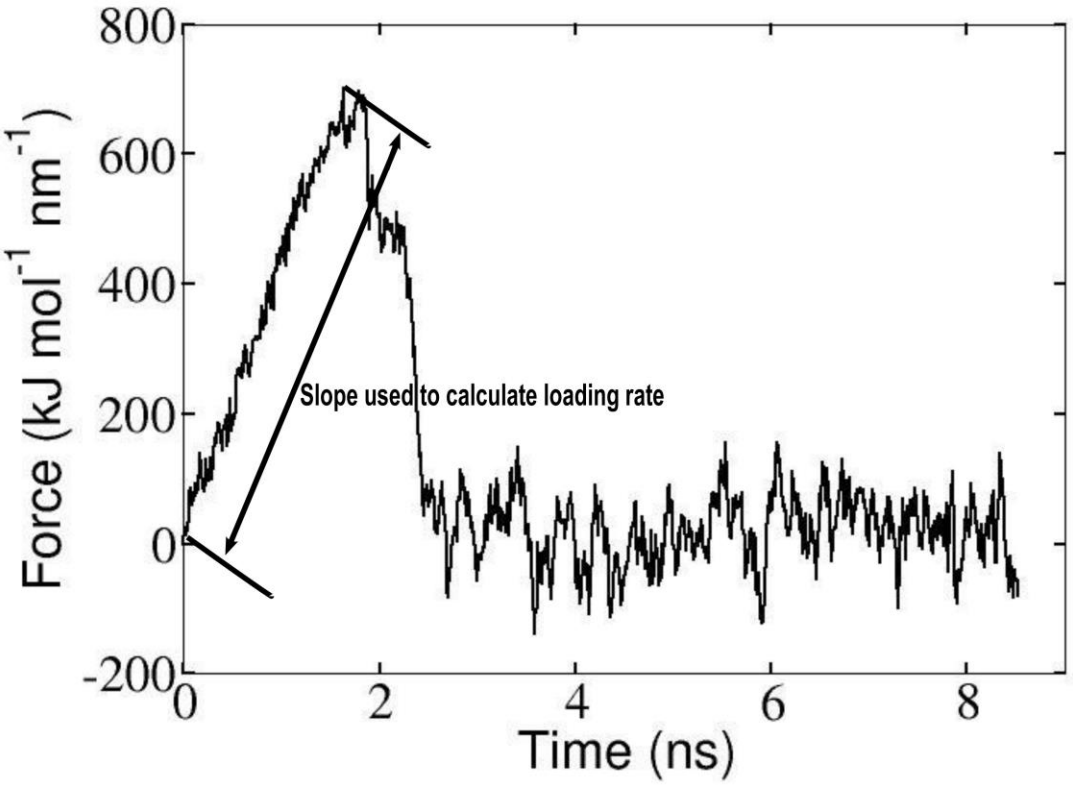

Figure 31

A typical SMD simulation showing the time evolution of force on the thrombin molecule, in MD simulation units. The information from this plot is utilized to calculate the loading rate associated with the corresponding simulation.

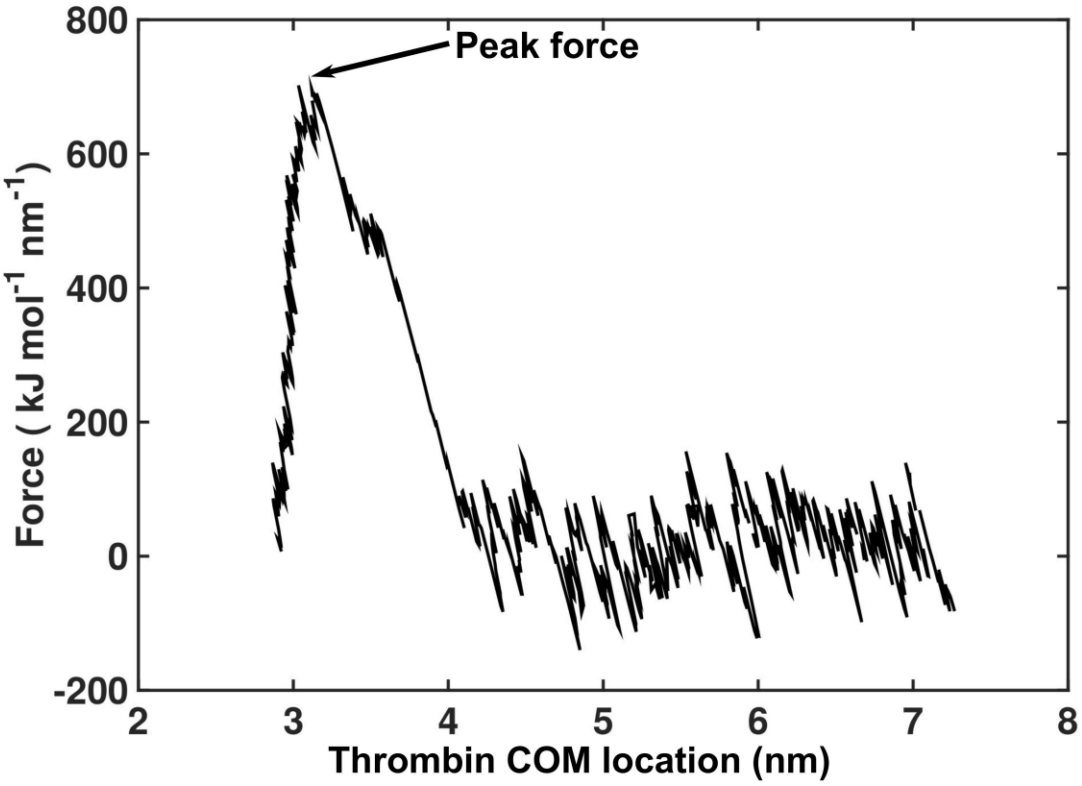

Figure 32

A typical SMD simulation showing the force on the thrombin molecule with increasing center of mass (COM) distance from the TBA, in MD simulation units